Subpicosecond vibronic dynamics in KBr F centers

Reinhard Scholz and Michael Schreiber
Institut für Physik, Technische Universität Chemnitz, D-09107 Chemnitz, Germany

Franco Bassani
Scuola Normale Superiore, Piazza dei Cavalieri 7, I-56126 Pisa, Italy

Mauro Nisoli, Sandro De Silvestri, and Orazio Svelto
Centro di Elettronica Quantistica e Strumentazione Elettronica, Politecnico di Milano, Piazza Leonardo da Vinci 32, I-20133 Milano, Italy

(Received 19 December 1996; revised manuscript received 26 March 1997)

Based on a symmetry analysis of recent results of femtosecond pump-probe optical-absorption experiments on KBr F centers, we present a twofold theoretical analysis. The first part is concerned with a density-matrix calculation of the experimentally observed beating pattern of two modes of A_{1g} symmetry in the sample transmission. This allows us to assign the observed frequencies to the breathing modes of the surrounding octahedron of cations in the electronic ground and excited state. The stiffening of the A_{1g} mode in the unrelaxed excited state is consistent with simple arguments based on a lattice of point charges. In the second part, the observed ultrafast loss of initial orientation of the excited p state is analyzed using a real-time integration of the wave function in the Hilbert space spanned by the vibrations of lower symmetries (E_{1g} and T_{2g}) and the three degenerate p states. The resulting reorientation of the p state can be regarded as the transient analogue of the Jahn-Teller effect, and it turns out that the total wave function loses its initial orientation on a very fast time scale. This phenomenon is interpreted as a loss of coherence, so that the breathing mode oscillation becomes observable only if the pulse length is of the order of the so-defined coherence time of $\tau_c = 12$ fs. [S0163-1829(97)00527-4]

I. INTRODUCTION

Recent advances in ultrafast laser sources have given the possibility to observe quantum oscillations in real time. After pioneering work on femtosecond dynamics of organic molecules,[1,2] ultrafast optical techniques have been used extensively for investigations of various transient quantum oscillations in solids. The observed phenomena range from pure lattice dynamics[3–8] over plasmon-phonon coupling[9,10] to pure electronic interference phenomena.[11–13] The phonon coupling mechanisms investigated include electronically induced displacement of the ion equilibrium coordinates in semimetals[3] and Fröhlich and deformation potential coupling in semiconductors.[4–8] Coherent phonons in high-T_c superconductors have revealed different dynamics in the superconducting and high-temperature range.[14]

While for all these pure crystalline materials the electron-lattice coupling is usually interpreted in terms of bulk phonons, defects or vacancies are strongly coupled to local lattice modes. A prototypical example is the color center in alkali halides, where an electron trapped in an anion vacancy interacts predominantly with the six even-parity modes of the surrounding octahedron of cations. This electron-lattice coupling leads to a Stokes shift of the order of 1 eV. In stationary absorption or photoluminescence, the corresponding lattice frequencies cannot be resolved[15] and Raman spectroscopy is needed for the identification of both the frequencies and symmetries.[16,17] From measurements under uniaxial stress, the contribution of lattice vibrations to the absorption linewidth can be estimated,[18] a fact that will be used in the following for the determination of the coupling parameters of each mode.

As both Raman and stress measurements reveal the predominance of breathing modes in the coupling of the color center absorption transition to vibronic excitations, the creation of a corresponding oscillatory wave packet must be possible with short enough light pulses. Recent experimental results obtained with a femtosecond pump-probe setup are reviewed briefly in Sec. II.[19] These data are analyzed using model calculations in the main part of the present work. The coupling parameters of the different symmetries are summarized in Sec. III, while details of the calculations are postponed to later sections. In Sec. IV, the linear optical response related to the breathing modes is calculated within a density-matrix approach. The resulting parameters are applied in Sec. V to the investigation of the nonlinear absorption saturation. The density-matrix calculation demonstrates that the observed oscillation is due to transient correlations between consecutive vibronic levels that have no equilibrium counterpart. Section VI deals with the modes of the lower E_{1g} and T_{2g} symmetries. A real-time integration of the excited-state wave function is performed, and consequences for the broadening mechanisms related to these modes are derived. The observed ultrafast loss of orientation of the excited electronic p state arises as a natural consequence of this analysis. In Sec. VII, we derive a condition for the observability of the A_{1g} oscillations, relating the pulse duration and coherence time of the excited-state wave function. This relation turns out to be much more restrictive than the condition for the observability of bulk phonons in other materials. The paper

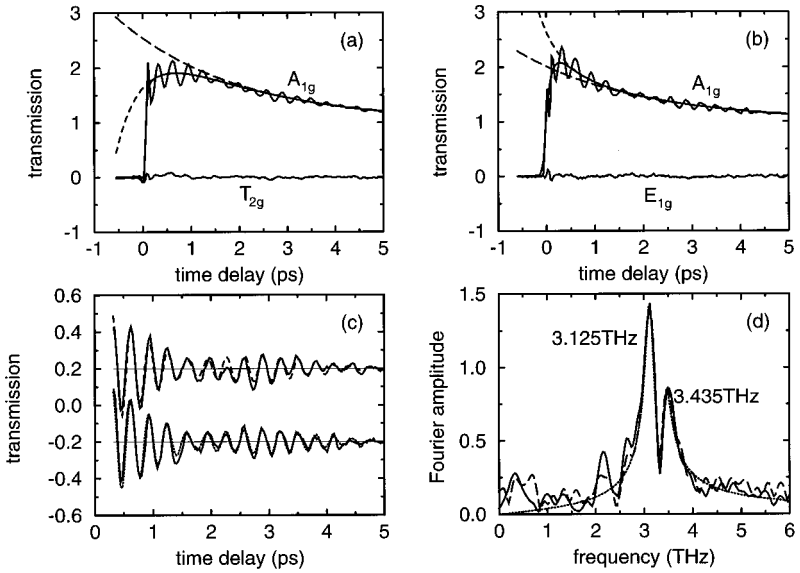

FIG. 1. Probe transmission change as a function of time delay between pump and probe pulse, for a thin sample of KBr containing $\approx 3\times 10^{16}$ cm^{-3} color centers. The photon energy is 1.75 eV, the pulse duration 15 fs, and the measurement was performed at room temperature. (a) Pump polarized at 45° to a cubic crystal axis. Upper solid line, measured A_{1g} signal; long-dashed line, exponential fit; short-dashed line, biexponential fit; smooth solid line, fit with exponential relaxation and smoothed step; lower line, signal of T_{2g} symmetry. Fit parameters for the nonoscillatory part of the A_{1g} signal: $t_0=30$ fs, $t_1=2.47$ ps, $t_2=0.55$ ps, $a_1=1.49$, and $a_2=-0.78$. (b) Like (a), but for the pump polarized along a cubic axis. The lowest line is the signal of E_{1g} symmetry. Nonoscillatory part: $t_0=125$ fs, $t_1=2.47$ ps, $t_2=0.40$ ps, $a_1=1.00$, and $a_2=0.58$. (c) Oscillatory part of data for delays greater than 320 fs. Solid lines, experimental; dashed line, two-oscillator fit for the pump at 45° to the cubic axis; dotted line, two-oscillator fit for pump along a cubic axis. The curves are shifted for clarity. (d) Amplitude Fourier spectrum of experimental signals in (c), with a superimposed fit for the pump polarized along a cubic axis. Solid line, experimental data for the pump at 45° to cubic axis; long-dashed line, experimental data for the pump along cubic axis; dotted line, corresponding fit. The fit for pump polarization at 45° to a cubic axis is skipped for clarity; its quality is similar to that for the other geometry; compare (c).

is summarized in Sec. VIII, and possible applications to similar systems are discussed.

II. EXPERIMENT

Transient pump-probe experiments were performed with pulses of 15-fs duration at 1.75-eV photon energy, corresponding to an energy uncertainty of 75 meV full width half maximum (FWHM). These pulses were obtained from 140-fs pulses of a Ti:sapphire laser by a recently developed compression technique.[19,20] The choice of the color center investigated was determined by the photon energy available with this system: At room temperature, the absorption line of the KBr F band is centered at 1.96 eV with a FWHM of about 0.34 eV,[15] so that the laser falls into the lower half. Probe transmission changes measured at room temperature are reported in Fig. 1 as a function of time delay between the pump and probe, normalized to the transmission change at long delay. The maximum transmission change corresponds to $\Delta T/T_0=(T-T_0)/T_0=0.4$.

For pump polarization along a cubic crystal axis or oriented at 45° to a cubic axis, we define signal contributions of A_{1g} symmetry by taking the *sum* of probe transmission for the probe polarized parallel to the pump field and orthogonal to it. The signals of the lower symmetries E_{1g} and T_{2g} are defined as the *difference*. There was virtually no contribution of the lower symmetries to the probe transmission within the noise limits, except for the first ≈ 100 fs after the pump. This demonstrates that the A_{1g} symmetry is dominating the transient dynamics of the optical absorption transition of the color center. These findings are in good agreement with the predominance of A_{1g} modes in stationary Raman signals[16,17] and their large contribution to the absorption linewidth.[18]

The nonoscillatory part of the A_{1g} probe transmission signal can be fitted with

$$(1-e^{-t/t_0})(1+a_1e^{-t/t_1}+a_2e^{-t/t_2}), \tag{1}$$

and the slowest time constant observed is $t_1=2.47$ ps for both pump polarizations, but with different amplitudes. Subtracting the fit yields the oscillatory part of the data shown in Fig. 1(c) together with a superimposed two-oscillator fit with

$$b_ge^{-t/\tau_g}\cos(\omega_gt+\phi_g)+b_ee^{-t/\tau_e}\cos(\omega_et+\phi_e), \tag{2}$$

where the frequencies ω_g and ω_e are related to the electronic ground and excited states, respectively. The two frequencies are obtained quite precisely with a nonlinear fitting procedure using Eq. (2): $\nu_g=\omega_g/2\pi=3.125\pm 0.006$ THz and $\nu_e=3.435\pm 0.010$ THz, corresponding to errors of 0.2% and 0.3%, respectively. These frequencies are in good agreement with low-temperature Raman modes of A_{1g} symmetry,[16,17] except for a temperature shift of -7%. As the A_{1g} modes fall into the region of the transverse optical phonon band, they will consist mainly of a coherent phase-matched superposition of optical phonons. The temperature dependence of the transverse optical phonon frequency in KBr was mea-

sured with neutron scattering and a rigid shift of the phonon band of -8% was found between $T=90$ K and $T=400$ K.[21,22] Our frequency shift of -7% between $T=10$ K and room temperature is consistent with these findings, and ω_g agrees well with the zone-center optical phonon energy at room temperature.[23] The reasons for the assignment of the measured frequencies to ground and excited states will become clear in the following sections.

Compared to the frequencies, all other fitted parameters are much less significant because different amplitudes, initial phases, and dephasing times can lead to reasonable agreement with the measured data. The dephasing times τ_g for the lower frequency ν_g agreed well for the two geometries, with an average of $\tau_g=1.80\pm0.15$ ps. For the higher frequency ν_e, the smaller amplitude leads to larger uncertainties: $\tau_e=2.28\pm0.4$ ps [upper curve in Fig. 1(c)] and $\tau_e=1.86\pm0.4$ ps [lower curve in Fig. 1(c)], with an average of 2.07 ± 0.3 ps. As expected, the room-temperature dephasing times are faster than values derived from the very small low-temperature Raman linewidth,[17] and the agreement with the broadening used in calculations of room-temperature microwave absorption is remarkable.[23] Despite the uncertainties of the fitted parameters, the agreement of the main features in Figs. 1(c) and 1(d) indicates that they are independent of excitation geometry.

The optical density of the sample can be used to derive the absorption change from the transmission change in Figs. 1(a) and 1(b). For $\hbar\omega=1.96$ eV, the energy of largest absorption of the *F* center at room temperature, the optical density due to the *F* center is about $\alpha_0 d=1.5$, which is reduced to about 0.8 in the energetic region of the femtosecond pulse. The initial oscillation amplitude in Figs. 1(a) and 1(b) is 0.22, and together with the normalization to the final value $\Delta T(t\rightarrow\infty)=0.4$, this gives an oscillation amplitude of $\Delta T_{\rm osc}=0.09$. Therefore, the relative change of the absorption coefficient can be estimated to be $\Delta\alpha_{\rm osc}/\alpha_0=0.09/0.8=0.11$. This indicates that the nonlinearity is small, so that a calculation to lowest order in the electric fields of the femtosecond pulses will be sufficient.

We have performed the same type of pump-probe experiment using longer pulses with a duration of the order of 80 fs. With these pulses, we did not find any oscillation amplitude above the noise level. The question of the observability of the oscillation pattern as a function of pulse length will be addressed in Sec. VI.

III. DETERMINATION OF MODEL PARAMETERS

A. Assignment of observed A_{1g} frequencies

The ground-state wave function of the electron trapped in the anion vacancy has *s* symmetry and a small spatial extension, so that the negative charge is mainly contained within the surrounding octahedron of cations.[24] As the charge of the electron and an anion is the same, the cations are close to their regular lattice positions. In the excited *p*-symmetric state, on the other hand, the electronic wave function is mainly localized outside the first shell of cations, even before excited-state lattice relaxation. This corresponds to a regular lattice where a positive point charge has been added in the position of the vacancy, so that the electron charge in the ground state is compensated, and an additional negative charge corresponding to the excited electronic state smeared out over a large region surrounding the octahedron of cations. The additional positive charge in the vacancy leads to a repulsive force on the cations, which will subsequently relax to a new equilibrium distance from the vacancy of about $r_e\approx1.1r_0$, where r_0 is the nearest-neighbor distance.[24] If the excitation is performed on a sufficiently fast time scale, the excited wave packet will perform an oscillation around this position.

For a qualitative argument concerning the vibrational frequencies, we model the ions as point charges and include the shifted positions of the cations of the first shell.[24] In the ground state, the potential energy of the A_{1g} breathing mode can be assumed to be parabolic, with a vibrating ground-state mass of six times the K^+ cation mass $m_g=6m_K$,

$$V_g(r)=\frac{m_g}{2}\omega_g^2(r-r_g)^2, \tag{3}$$

where r is the distance of the cations from the vacancy and $r_g\approx0.98r_0$ their equilibrium position.[24] Because this is very close to the regular lattice position, the bulk vibrations remain nearly undisturbed and the frequency ω_g agrees quite well with the optical phonon energy at room temperature.[23] The excited-state vibronic potential has to include the Coulomb interaction of the six cations with the positive charge at the origin:

$$V_e(r)=V_g(r)+\frac{6e^2}{4\pi\epsilon_0 r}. \tag{4}$$

Calculating the curvature of this potential in the position of the cations, we can identify the excited-state frequency ω_e and mass m_e:

$$\frac{\partial^2}{\partial r^2}V_e(r)=m_g\omega_g^2+\frac{6e^2}{2\pi\epsilon_0 r^3}=m_e\omega_e^2. \tag{5}$$

Using the above values for m_g and r_g and the new equilibrium position $r_e=1.1r_0$,[24] with $r_0=3.29$ Å, we arrive at the ratio of curvatures

$$\frac{m_e\omega_e^2}{m_g\omega_g^2}=1.39, \tag{6}$$

which indicates a stiffening of the vibrational frequency in the excited state. Taking the higher measured frequency of 3.435 THz as the excited-state frequency and 3.125 THz as the ground-state frequency, we find that a mass ratio of about $m_e/m_g=1.16$ is needed to reconcile the measured data and the above point-charge arguments. Further corrections arise because the ground-state wave function is not fully contained within the shell of the cations and the excited electronic wave function does not have all its charge density outside this shell. Calculations in the literature indicate that the optical excitation yields a change of the charge within the nearest-neighbor shell remaining somewhat smaller than e.[24,25] Therefore, the ratio $m_e\omega_e^2/m_g\omega_g^2$ is further reduced, still remaining higher than one. The assignment of the ground- and excited-state frequencies is not affected, but the ratio of the masses becomes closer to one.

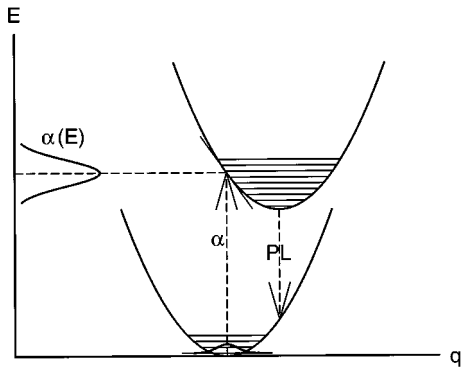

FIG. 2. Schematic configuration coordinate diagram for a single oscillator with a displaced minimum in the upper state. $\alpha(E)$, absorption line shape; PL, photoluminescence.

From these arguments it is not evident that a parabolic potential for the excited state is still realistic, as the additional Coulomb part is certainly far from parabolic. The evidence is indirect: Calculating the optical absorption line shape with a nonparabolic Morse potential for the excited state along the lines indicated in Sec. IV, we arrive at the best agreement with the measured line shape[15] if the nonparabolicity is very small. The rearrangement of the disturbed lattice to a nearly parabolic potential for the breathing mode can be due to small changes of the ionic positions in the consecutive shells surrounding the octahedron of cations. A detailed knowledge of the ion-ion potential including a realistic repulsive part would be needed for more precise calculations.[26] For the ground- and excited-state Hamiltonians, we take the minimum of the ground-state potential as the origin of the oscillator coordinate $q=r_g-r_0$ and assume parabolic potentials:

$$H_g(A_{1g})=\frac{p^2}{2m_g}+\frac{m_g}{2}\omega_g^2 q^2+E_s,$$

$$H_e(A_{1g})=\frac{p^2}{2m_e}+\frac{m_e}{2}\omega_e^2(q-q_0)^2+E_p. \tag{7}$$

The corresponding potentials are sketched schematically in the so-called configuration coordinate diagram in Fig. 2. As the point-charge arguments indicate that the mass difference should be small, we use the same mass in the ground and excited state $m_g=m_e=6m_K$. The lower frequency is assigned to the ground state $\omega_g=\nu_g/2\pi=19.6/\text{ps}$ and the higher frequency to the excited state $\omega_e=\nu_g/2\pi=21.6/\text{ps}$. E_s and E_p are the energies of the electronic ground and excited states. The elongation $q_0=0.21$ Å$=0.064r_0$ between the minima of the excited- and ground-state potentials is determined from the contribution of the A_{1g} symmetry to the linewidth, as discussed in the following subsection and Sec. IV in some detail. The difference of the electronic energies turns out to be $E_p-E_s=1.712$ eV at room temperature.

The use of the above parameters for luminescence from the relaxed excited state of the color center would be misleading because its electronic wave function has a much larger extension, corresponding also to a larger elongation q_0.[24] In principle, the photoluminescence transition in Fig. 2 should start from the potential-energy surface of the relaxed excited state, which in general will not coincide with the upper-state potential governing optical absorption from the ground-state minimum. As we will never be concerned with details of the optical coupling from the relaxed excited state towards the ground state in this paper, we have not shown the corresponding relaxed excited-state potential in Fig. 2 for clarity.

B. Line-shape analysis

In the present subsection we summarize the coupling parameters of the vibronic modes derived in the calculations in Secs. IV and VI. The vibronic modes coupling linearly to the color center transition are easily found by analyzing the representations in the cubic point group. The representations corresponding to electronic s and p states are A_{1g} and T_{1u}, respectively. The vibronic modes with linear coupling to the p state are found from the product of its representation in the cubic group with itself:[27]

$$T_{1u}T_{1u}=A_{1g}+E_{1g}+T_{2g}+\mathcal{R}, \tag{8}$$

where $\mathcal{R}$ denotes rotations. Furthermore, the excited p state can be mixed with an s state close in energy via modes of T_{1u} symmetry. The role of this so-called pseudo-Jahn-Teller effect seems to be unclear for the color center in alkali halides, as the crucial absorption experiment seems to be missing.[28] We will ignore any effect related to these pseudo-Jahn-Teller modes in the following because it is generally accepted that this effect is unimportant during absorption, the $2p$ state being below the $2s$ state.[29]

The neglect of the pseudo-Jahn-Teller effect would be unwise for transient experiments concerning the relaxed excited state because there is strong evidence that the $2s$ state is slightly below the $2p$ state. This is demonstrated by various investigations of F-center photoluminescence, such as the temperature dependence of the excited-state lifetime,[30] wave-function calculations,[31] and calculations of the pseudo-Jahn-Teller effect.[32,33] The latter calculations did not include the pseudo-Jahn-Teller modes of T_{1u} symmetry and the Jahn-Teller modes of E_{1g} and T_{2g} symmetries on an equal footing. Early experiments on luminescence under stress were interpreted in a much simpler model neglecting the $2s$ states completely.[34]

Because of the simpler ordering of the $2s$ and $2p$ states during optical absorption, $E_{2p}<E_{2s}$, the pseudo-Jahn-Teller effect due to the T_{1u} modes should be of minor importance compared to the influence of the even modes. Using pressure and uniaxial stresses, the contributions of A_{1g}, E_{1g}, and T_{2g} symmetry to the second moment of the absorption line can be obtained.[18,35] This does not give information on the detailed line shape, but the absorption line is approximately Gaussian, $\alpha(E)=\exp[-(E-E_0)^2/a^2]$, so that second moment $\langle E^2\rangle$ and FWHM W are given by $\langle E^2\rangle=a^2/2$ and $W=2\sqrt{\ln 2}a$. Modes of different symmetries are assumed to be independent and each mode alone is expected to give a Gaussian line shape. Therefore, their contributions to total second moment and linewidth add in the same way,

$$\langle E^2\rangle=\langle E^2(A_{1g})\rangle+\langle E^2(E_{1g})\rangle+\langle E^2(T_{2g})\rangle+\langle E^2(\text{so})\rangle,$$

TABLE I. Contributions to second moment and width of the absorption line. A_{1g}, E_{1g}, and T_{2g} denote the corresponding vibrational symmetries and so denotes spin-orbit splitting. The effective mode frequencies assumed for the E_{1g} and T_{2g} symmetries are written in *italics*. The values for zero and room temperature are derived from the measurements of the second moment at $T=80$ K (Ref. 18).

Symmetry/T (K)	$\langle E^2\rangle$ (meV^2) 80	W (meV)	W (meV) 0	W (meV) 300	$\hbar\omega$ (meV)
A_{1g}	$(73\pm7)^2$	172 ± 16	147	298	12.9
E_{1g}	$(19\pm2)^2$	45 ± 5	35	81	*10.*
T_{2g}	$(29\pm3)^2$	68 ± 7	54	123	*10.*
E_{1g} and T_{2g}	$(35\pm4)^2$	82 ± 9	64	147	*10.*
so	14^2	33	33	33	
E_{1g} and T_{2g} and so	$(37\pm4)^2$	88 ± 9	72	151	12.1
total (Expt.)[a]	82^2	193			
total (Expt.)[b]		191	158	337	11.6
total (Calc.)	82^2	193	164	334	12.7

[a]Reference 18.
[b]Reference 36.

$$W^2=W^2(A_{1g})+W^2(E_{1g})+W^2(T_{2g})+W^2(\mathrm{so}), \qquad (9)$$

and the relative contributions are equal. The last term in each case is due to spin-orbit splitting. The contributions to second moment[18] and linewidth at $T=80$ K are given in the second and third columns of Table I. To the best of our knowledge, the measurement of the second moments has not been repeated for different temperatures. Therefore, we need further parameters for the extrapolation from $T=80$ K to zero and room temperature. The temperature-dependent linewidth for a single oscillator with the same frequency ω in the ground and excited states is known to be[15]

$$W(T)=W(0)\left[\coth\left(\frac{\hbar\omega}{2k_BT}\right)\right]^{1/2}. \qquad (10)$$

Using the measured temperature dependence, $W(0)=158$ meV, and an effective vibronic energy of $\hbar\omega=11.6$ meV,[36] we arrive at $W(80\ \mathrm{K})=191$ meV, in good agreement with the total linewidth of $W(80\ \mathrm{K})=193$ meV derived from the second moment of the absorption line; compare Table I. In the following, we use the slightly higher total linewidth,[18] the difference of 2 meV being well within the experimental errors.

For the A_{1g} modes, the line shape as a function of temperature is calculated explicitly in Sec. IV from the above Hamiltonian (7). The resulting width is fitted according to Eq. (10) with an A_{1g} mode energy of $\hbar\omega(A_{1g})=12.9$ meV, corresponding to the ground-state frequency entering the Hamiltonian.

Raman experiments on the KBr F center indicate one-phonon structures of E_{1g} and T_{2g} symmetry between 6 and 20 meV.[16] In the following, we assume that effective vibronic energies of 10 meV describe the contribution of these modes to the temperature-dependent linewidth, an energy within the range observed in Raman experiments. Such an approach is known as the quasimolecular (cluster) model.[37]

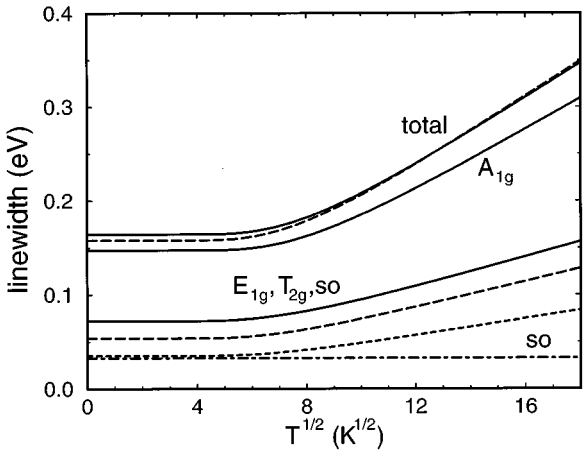

FIG. 3. Contributions of different vibrational symmetries and spin-orbit splitting to the total linewidth. From bottom to top: spin-orbit splitting (short-dashed–long-dashed line), E_{1g} symmetry (short-dashed line), T_{2g} symmetry (long-dashed line), E_{1g} and T_{2g} symmetries and spin-orbit splitting together (solid line), A_{1g} symmetry (solid line), total linewidth [solid line, calculated from the contributions of different symmetries; long-dashed line, experimental linewidth (Ref. 38)].

The resulting low- and high-temperature linewidths are calculated with Eq. (10) and the vibronic energies in Table I. The assumption that the modes of lower symmetries have energies below the breathing mode is in qualitative agreement with a temperature-dependent determination of the second and third moments of the absorption line for KCl.[38]

The linewidth resulting from the different symmetries is shown in Fig. 3, where the spin-orbit splitting is assumed to be temperature independent. The breathing modes give a dominating contribution to the total linewidth for all temperatures. This is a peculiarity of the F center in the NaCl structure, while substitutional cations such as In^+ and Tl^+ in the same crystals have similar contributions from the breathing modes and the modes of lower symmetry to the total linewidth.[28] The opposite extreme is the F^+ absorption band in CaO, where the breathing modes merely lead to a smoothing of the structure determined by the E_{1g} and T_{2g} Jahn-Teller modes.[39,40]

Because the breathing modes dominate the linewidth, they will be treated separately from the modes of lower symmetry in Secs. IV and V, with the influence of the other modes included phenomenologically. Therefore, it is useful to divide the total linewidth into the contribution of the A_{1g} modes and the rest composed of contributions of E_{1g} and T_{2g} symmetries and spin-orbit splitting. The inclusion of spin-orbit splitting in the remaining part of the linewidth increases its effective mode energy because of the temperature independence of the splitting; compare Table I.

The total calculated linewidth coincides with the linewidth measurements within ±6 meV for all temperatures, which is within the experimental uncertainties. The derived effective vibronic energy of 12.7 meV is already considerably higher than the experimental one[36] because the low- and high-temperature deviations between the calculated and the measured linewidth have opposite sign. Among the possible systematic errors of the calculation is the assumption of temperature-independent vibronic energies, while the experi-

mental results in Sec. II indicate a shift of the A_{1g} modes of -7% between $T=10$ K (Ref. 17) and room temperature. Furthermore, the vibrating mass was assumed to be the same in the electronic ground and excited states. Erroneous assignments of the modes of E_{1g} and T_{2g} symmetries should not have a large influence on the total linewidth as a function of temperature, as these modes are only of minor importance at $T=80$ K.

The high-temperature linewidth contributions are supposed to be exact within an uncertainty range of $\pm 15\%$, somewhat higher than the experimental range of $\pm 10\%$ given for the measurement of the second moment at $T=80$ K. As the linewidth is linear in the elongation between ground and excited states, the uncertainty of 15% applies also to the elongations of the different modes. The above parameters will be used in Secs. IV and V for the calculation of the A_{1g} modes and in Sec. VI for the E_{1g} and T_{2g} modes.

IV. DENSITY-MATRIX CALCULATION FOR BREATHING MODES

A. Hamiltonian for breathing modes

For the following investigation of linear and nonlinear optics, we express all operators in terms of projectors on the eigenstates corresponding to the Hamiltonian (7) and the configuration coordinate diagram Fig. 2. The eigenstates are denoted $|s,i\rangle=|s\rangle\otimes|i_g\rangle$ for the electronic ground state and $|x,j\rangle=|x\rangle\otimes|j_e\rangle$, $|y,j\rangle=|y\rangle\otimes|j_e\rangle$, and $|z,j\rangle=|z\rangle\otimes|j_e\rangle$ for the electronic excited state. On the right-hand side (rhs), the first part in each case is the electronic wave function, $|i_g\rangle$ a vibrational level in the ground-state oscillator potential, and $|j_e\rangle$ a vibrational level in the upper-state potential. Expressed in terms of projectors on its eigenstates, the above Hamiltonian for the breathing modes, Eq. (7), is expressed as

$$\hat{H}_0(A_{1g})=\sum_i \hbar\omega_{gi}|s,i\rangle\langle s,i| + \sum_j \hbar\omega_{ej}(|x,j\rangle\langle x,j|+|y,j\rangle\langle y,j|+|z,j\rangle\langle z,j|), \tag{11}$$

where the abbreviations $\omega_{gi}=E_s/\hbar+(i+1/2)\omega_g$ and $\omega_{ej}=E_p/\hbar+(j+1/2)\omega_e$ have been used. In the above form, the Hamiltonian applies also to nonparabolic potentials for the breathing mode; only the frequencies ω_{gi} and ω_{ej} would be defined in a different way. In the following, we will reserve the indices i and k for the ground-state vibronic levels and j and l for the excited levels.

For the coupling to the electric field of the optical pulse, we use the Hamiltonian

$$\hat{H}_{\rm opt}(A_{1g})=-E_x(t)\hat{\mu}_x(A_{1g},t)+(y,z) = -E_x(t)d\sum_{i,j}(|x,j\rangle\langle s,i|F_{ji}+|s,i\rangle\langle x,j|F_{ij}) + (y,z), \tag{12}$$

where $E_x(t)$ is the electric field of the light pulses, $\hat{\mu}_x(A_{1g},t)$ the operator of the time-dependent dipole moment of the transition, and $d=\langle s|x|x\rangle$ the dipole matrix element between the electronic ground and excited states. The sum contains the projection of the wave functions of the vibrational levels in the electronic ground state on the vibrational levels of the electronic excited states and $F_{ji}=\langle j_e|i_g\rangle$ is an abbreviation for the Franck-Condon overlap factor of the oscillator wave functions. The Franck-Condon factors are calculated with the standard eigenfunctions of the harmonic oscillator, which we assume to be real.[41] The coupling to electric fields along the y and z axes has to be included in the same way in the Hamiltonian $\hat{H}_{\rm opt}(A_{1g})$.

B. Equations of motion for the observables

The density-matrix approach consists of investigating equations of motion for operators, usually based on the eigenstates of the unperturbed system.[42] The operators of interest include, e.g., $|x,j\rangle\langle s,i|$, the transition from $|s\rangle\otimes|i_g\rangle$ to $|x\rangle\otimes|j_e\rangle$; $|x,j\rangle\langle x,j|$, the occupation of $|x\rangle\otimes|j_e\rangle$; and $|x,j\rangle\langle x,k|$, the correlation of $|x\rangle\otimes|j_e\rangle$ and $|x\rangle\otimes|k_e\rangle$. Calculating the commutators of these operators $\hat{O}$ and the Hamiltonian $\hat{H}(A_{1g})=\hat{H}_0(A_{1g})+\hat{H}_{\rm opt}(A_{1g})$, we arrive at the following equations of motion for the ensemble average of the expectation value:[42]

$$\frac{\partial}{\partial t}\langle\hat{O}\rangle=\frac{1}{i\hbar}\langle[\hat{O},\hat{H}(A_{1g})]\rangle+\frac{d}{dt}\langle\hat{O}\rangle_{\rm irr}, \tag{13}$$

where the last term describes the irreversible contributions phenomenologically, usually the coupling to the surrounding bath of other lattice modes. The angular brackets in Eq. (13) stand for

$$\langle\hat{O}\rangle={\rm Tr}(\hat{\rho}^{(0)}\hat{O}), \tag{14}$$

where $\hat{\rho}^{(0)}$ is the equilibrium density matrix. $\hat{\rho}^{(0)}$ contains, on the diagonal, thermal occupations of the vibrational levels corresponding to the electronic ground state, while occupations in the excited state and off-diagonal elements vanish,

$$\rho^{(0)}_{\alpha i,\beta k}=\delta_{\alpha s}\delta_{\alpha\beta}\delta_{ik}n^{(0)}_{gi}, \tag{15}$$

with the thermal occupation $n^{(0)}_{gi}$ of the vibrational levels according to Bose-Einstein statistics:

$$n^{(0)}_{gi}=c(T)\exp\left(-\frac{\hbar\omega_{gi}}{k_BT}\right). \tag{16}$$

$c(T)$ is a temperature-dependent normalization constant, so that the sum over all vibrational levels gives unity. The temporal dynamics arises from the perturbation by the electric field in the Hamiltonian for the optical transition, Eq. (12). Time-dependent ensemble averages of operators are expressed as

$$\rho_{\alpha i,\beta j}(t)={\rm Tr}(\rho^{(0)}|\alpha,i\rangle\langle\beta,j|) \tag{17}$$

and set up the time-dependent density matrix for the system perturbed by the electric field. For the transitionlike matrix elements between the ground and excited states, we arrive at the set of equations of motion

$$\left(\frac{\partial}{\partial t}-i(\omega_{ej}-\omega_{gi})\right)\rho_{xj,si}(t)$$
$$=\frac{id}{\hbar}E_x(t)\left(\sum_l F_{il}\rho_{xj,xl}(t)-\sum_k F_{kj}\rho_{sk,si}(t)\right)$$
$$+\frac{id}{\hbar}E_y(t)\sum_l F_{il}\rho_{xj,yl}(t)+\frac{id}{\hbar}E_z(t)\sum_l F_{il}\rho_{xj,zl}(t)$$
$$+\frac{d}{dt}[\rho_{xj,si}(t)]_{\rm irr}. \tag{18}$$

The saturation terms on the rhs describe Pauli blocking of the transition between the ground and excited states. The equations of motion for the correlations between different vibrational levels $|l_e\rangle$ and $|j_e\rangle$ in the upper-state potential for the same p state $|x\rangle$ read

$$\left(\frac{\partial}{\partial t}-i(\omega_{ej}-\omega_{el})\right)\rho_{xj,xl}(t)$$
$$=\frac{id}{\hbar}E_x(t)\left(\sum_k F_{lk}\rho_{xj,sk}(t)-\sum_k F_{kj}\rho_{sk,xl}(t)\right)$$
$$+\frac{d}{dt}[\rho_{xj,xl}(t)]_{\rm irr}. \tag{19}$$

For the diagonal case $|l_e\rangle=|j_e\rangle$, this formula describes simply the occupation. A similar equation of motion can be obtained for the correlations between different vibrational levels in the electronic ground state $|s\rangle\otimes|i_g\rangle$ and $|s\rangle\otimes|k_g\rangle$:

$$\left(\frac{\partial}{\partial t}-i(\omega_{gk}-\omega_{gi})\right)\rho_{sk,si}(t)$$
$$=\frac{id}{\hbar}E_x(t)\left(\sum_l F_{il}\rho_{sk,xl}(t)-\sum_l F_{lk}\rho_{xl,si}(t)\right)$$
$$+(y,z)+\frac{d}{dt}[\rho_{sk,si}(t)]_{\rm irr}. \tag{20}$$

C. Linear optics

For the calculation of the linear response of the color center transition, we can assume that the electronic ground state is occupied with unit probability $n_s^{(0)}=\Sigma_i n_{gi}^{(0)}=1$ and a distribution over the levels according to Bose-Einstein statistics, Eq. (16). As an ansatz for the irreversible part of the equation of motion for the transition matrix elements, Eq. (18), we use an infinitesimal decay rate $\Gamma=0^+$. With a Fourier transformation $t\rightarrow\omega$, we arrive at the linear response of the transition matrix elements

$$\rho_{xj,si}^{(1)}(\omega)=\frac{dF_{ij}n_{gi}^{(0)}}{\hbar[\omega_{ej}-\omega_{gi}+\omega+i\Gamma]}E_x(\omega), \tag{21}$$

where the linearity in the field is expressed by the superscript (1). The resulting polarization response is given by the density of dipole moments $\mu(A_{1g},\omega)=\langle\hat{\mu}(A_{1g},\omega)\rangle$,

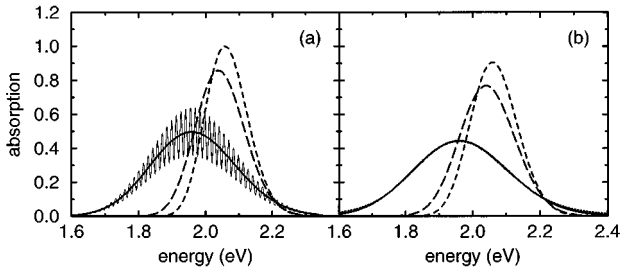

FIG. 4. (a) Absorption line shape due to A_{1g} modes alone, calculated with an elongation $q_0=0.064r_0$. A Gaussian broadening with $W=20$ meV is included for the three temperatures $T=0$ K (short-dashed line), $T=80$ K (long-dashed line), $T=300$ K (solid line). For $T=300$ K, a curve calculated with smaller Gaussian broadening of $W=10$ meV is shown for comparison (oscillating line). The data are normalized to the peak absorption at zero temperature. (b) Same as (a), but with the broadening parameters of Table I: $W=72$ meV ($T=0$ K), 88 meV ($T=80$ K), and 151 meV ($T=300$ K). For $T=300$ K, a dotted line is calculated with Lorentzian broadening using a dephasing time of $T_2=22$ fs. The peak position in (a) and (b) is due to a temperature dependence of the electronic energies in the calculation: $E_p-E_s=1.812$ ($T=0$ K), 1.732 ($T=80$ K), and 1.712 ($T=300$ K), which reproduces the experimental peak positions $E(\alpha_{\rm max})=2.06$ eV ($T=0$ K), 2.04 eV ($T=80$ K), and 1.96 eV ($T=300$ K); compare Ref. 15.

$$P_x^{(1)}(A_{1g},\omega)$$
$$=n_F d\sum_{i,j}[F_{ji}\rho_{xj,si}^{(1)}(\omega)+F_{ij}\rho_{si,xj}^{(1)}(\omega)]$$
$$=\frac{n_F}{\hbar}\sum_{i,j}\left[\frac{n_{gi}^{(0)}d^2F_{ji}^2}{\omega_{ej}-\omega_{gi}+\omega+i\Gamma}+\frac{n_{gi}^{(0)}d^2F_{ij}^2}{\omega_{ej}-\omega_{gi}-\omega-i\Gamma}\right]$$
$$\times E_x(\omega), \tag{22}$$

where n_F is the density of color centers. For positive frequency, the first term is antiresonant, so that it can be neglected in the imaginary part of the dielectric response $\epsilon^{(1)}(A_{1g},\omega)=P_x^{(1)}(A_{1g},\omega)/\epsilon_0 E_x(\omega)$ near the resonance:

$$\mathrm{Im}\epsilon^{(1)}(A_{1g},\omega)=\frac{n_F}{\hbar\epsilon_0}\sum_{i,j}\mathrm{Im}\frac{n_{gi}^{(0)}d^2F_{ji}^2}{\omega_{ej}-\omega_{gi}-\omega-i\Gamma}. \tag{23}$$

Furthermore, each transition frequency between breathing mode vibrational levels $\omega_{ej}-\omega_{gi}$ is broadened by a Gaussian related to E_{1g} and T_{2g} modes and spin-orbit splitting,

$$\mathrm{Im}\epsilon^{(1)}(\omega)=\int d\omega'\,\mathrm{Im}\epsilon^{(1)}(A_{1g},\omega')\exp\left(-\frac{(\omega-\omega')^2}{a^2}\right), \tag{24}$$

with the corresponding broadening parameters for different temperatures in Table I.

The resulting absorption line shape due to the A_{1g} modes is given in Fig. 4(a) for three different temperatures, normalized to the peak value at $T=0$ K. The Gaussian broadening of the transition frequencies is set to $W=20$ meV, enlarging the width of the absorption line by about 1%. Already with this small broadening, the different A_{1g} transition frequencies are invisible. As the total oscillator strength of the color

center transition is temperature independent within our model, the increase of the linewidth with temperature leads to a decrease of the peak absorption. The absorption at $T=300$ K is also shown with a smaller broadening of $W=10$ meV for comparison and the different transitions are clearly visible. This case is obviously unrealistic for the F center under study, but different centers can indeed allow one to observe distinct vibronic peaks superimposed on a smooth absorption line.[43]

Figure 4(b) contains the absorption line including the temperature-dependent width resulting from E_{1g} and T_{2g} modes and spin-orbit splitting according to the parameters in Table I. The increase of the linewidth is about 10%, so that the absorption maximum decreases by the same amount; compare Fig. 4(a). A similar absorption line shape can be obtained with a finite dephasing rate $\Gamma=1/22$ fs and no Gaussian broadening, as shown for room temperature in Fig. 4(b). The main deviations are far off the resonance. For simplicity, we will use the finite dephasing rate Γ in Sec. V, avoiding the more involved inclusion of Gaussian broadening in the calculation of the nonlinear response.

Only the frequency of the ground-state oscillator enters the temperature dependence of the A_{1g} linewidth according to Eq. (10), while the vibrational levels corresponding to the electronic p states act merely as a complete set of basis functions without any influence on the linewidth. For the photoluminescence, the reverse is true, but we do not claim that the same parameters for the breathing mode potentials apply, as it is known that the relaxed excited p state has a much larger radial extension.[24] Therefore, the electronic charge density entering the potential of the breathing modes will be different for recombination starting near the minimum of the excited state potential and all parameters entering the breathing mode Hamiltonian will be changed. This is probably the reason why our elongation $q_0=0.064r_0$ between ground- and excited-state minima is much smaller than the value $q_0=0.12r_0$ calculated for the relaxed excited p state.[24] Many features of the recombination can be modeled along similar lines, such as the temperature dependence of the linewidth.[44] Because of the ordering $E_{2s}<E_{2p}$ for the relaxed excited state, the detailed assignment of model parameters would be somewhat more involved than in Sec. III.

V. CALCULATION OF NONLINEAR TRANSMISSION CHANGE

The aim of the present section is to calculate the nonlinear dynamics of the A_{1g} modes observed in the transmission of the probe pulse. In the configuration coordinate scheme in Fig. 2, the ultrafast optical excitation projects the wave function of the occupied ground-state vibrational level on the upper parabola, where a superposition of eigenstates is created. Their subsequent oscillation in the upper potential leads to a recurrence of the wave packet after integer multiples of the oscillation period $t=nT_{\rm osc}$. Only then can the wave packet influence the optical coupling, while after half-integer multiples of the oscillation period $t=(n+1/2)T_{\rm osc}$, the wave packet is on the rhs of the upper potential and does not saturate the optical transition for photon energies coupling resonantly on the lhs of the upper potential. In the lower potential, a similar oscillation occurs when the coupling to the pump pulse leads to a transition between subsequent vibrational levels. This phenomenon is not so obvious as the oscillation of the wave packet in the upper potential, but follows directly from the calculation developed below.

The density-matrix approach is best suited for modeling these dynamics, as it allows us to treat coherence and dephasing without problems concerning the conservation of the total probability: Oscillations are due to off-diagonal elements of the density matrix, while charge conservation is related to the time independence of its trace.

In the following, we have to identify the most important saturation terms in the equations of motion for the transitions, Eq. (18), after the pump pulse has arrived on the sample. In this case, the electric field on the rhs will be the probe field and the quantum dynamics induced by the pump pulse is included in the ensemble averages $\rho_{xj,xl}$, etc., on the rhs. As will become clear in the following discussion, the leading order of changes in these source terms is quadratic in the electric field of the pump pulse and the calculation we will develop in this section is a typical application of density-matrix theory.[45]

The dynamics of the modes of lower symmetry is approximated in this section by simple terms for the irreversibilities of the A_{1g} modes: The broadening discussed in Fig. 4(b) is obtained now with a dephasing rate $\Gamma=1/22$ fs. The difference between the assumed Lorentzian broadening and the correct Gaussian broadening will lead only to minor quantitative changes in the response to a short pulse, as the time dependences are mainly determined by the pulse envelope with intensity FWHM of 15 fs.

Before the experiment is performed, the electron in the color center is in its ground state $|s\rangle$ with unit probability $n_s^{(0)}=1$. The first step is to calculate the transitions induced by the pump field, and because of $n_s^{(0)}=1$, only one term on the rhs of Eq. (18) contributes, while all others vanish. The resulting transition matrix elements are calculated as in Sec. IV B, but now with the electric field of the pump pulse, which is assumed to be x polarized. It is convenient to express the pump field as a product of the envelope and phase

$$\mathbf{E}^{\rm pu}(t)=E^{\rm pu}(t)\mathbf{e}_x$$

$$=\tilde{E}^{\rm pu}(t)(e^{-i\omega^{\rm pu}t}+e^{i\omega^{\rm pu}t})\mathbf{e}_x\,. \tag{25}$$

The shape of the envelope $\tilde{E}^{\rm pu}(t)$ is taken to be $\mathrm{sech}(t/\tau)$ with $\tau=15$ fs$/2\ln(\sqrt{2}+1)$ corresponding to the pulse duration of a FWHM equal to 15 fs. For the photon energy, we use the experimental value of $\hbar\omega^{\rm pu}=1.75$ eV. Because of the pulsed field of the pump laser, it is most convenient to express the linear response as a time integration over the past

$$\rho^{(1)}_{xj,si}(t)=-\frac{id}{\hbar}n^{(0)}_{gi}F_{ij}e^{i\omega^{\rm pu}t}$$

$$\times\int_{-\infty}^{t}dt'\,e^{i[\omega_{ej}-\omega_{gi}-\omega^{\rm pu}](t-t')}e^{-\Gamma(t-t')}\tilde{E}^{\rm pu}(t')$$

$$+\mathcal{A}(\omega_{pu}\rightarrow-\omega_{pu}), \tag{26}$$

where $\mathcal{A}$ denotes the antiresonant term. Even for energetically broad pulses of 15-fs duration, the antiresonant term gives a very small contribution to the absorption because the detuning $\omega_{ej}-\omega_{gi}+\omega^{\mathrm{pu}}$ is large for all transition energies $\omega_{ej}-\omega_{gi}$.

The transition matrix elements linear in the pump field are then used in the source terms of the equation of motion for correlations between vibrational states, i.e., Eq. (19) for the oscillator potential corresponding to the excited electronic state $|x\rangle$. Up to second order in the pump field, we obtain the equation of motion

$$\left(\frac{\partial}{\partial t}-i(\omega_{ej}-\omega_{el})\right)\rho^{(2)}_{xj,xl}(t) = \frac{id}{\hbar}E^{\mathrm{pu}}(t)\left(\sum_k F_{lk}\rho^{(1)}_{xj,sk}(t)-\sum_k F_{kj}\rho^{(1)}_{sk,xl}(t)\right) + \mathcal{I}, \tag{27}$$

where $\mathcal{I}$ denotes irreversible terms, and similarly for the correlations between vibrational levels in the electronic ground state, $|s\rangle\otimes|i_g\rangle$ and $|s\rangle\otimes|k_g\rangle$:

$$\left(\frac{\partial}{\partial t}-i(\omega_{gk}-\omega_{gi})\right)\rho^{(2)}_{sk,si}(t) = \frac{id}{\hbar}E^{\mathrm{pu}}(t)\left(\sum_l F_{il}\rho^{(1)}_{sk,xl}(t)-\sum_l F_{lk}\rho^{(1)}_{xl,si}(t)\right) + \mathcal{I}. \tag{28}$$

The quality of the approximation to iterate only up to second order in the pump field depends on the excitation density. As discussed in Sec. II, the oscillating part of the absorption coefficient corresponds to a relative change of $\Delta\alpha_{\mathrm{osc}}/\alpha_0=11\%$. As this is much smaller than one, the main features should be obtained already in the lowest order in the pump field.

The most important terms for the nonlinear probe transmission are the occupations of vibrational levels and the first off-diagonal correlations $j-l=\pm 1$ oscillating with $\omega_{ej}-\omega_{el}=\pm\omega_e$ and $k-i=\pm 1$ oscillating with $\omega_{gk}-\omega_{gi}=\pm\omega_g$. These nondiagonal terms are not subject to any conservation law, so that simple dephasing rates $\Gamma_g=1/\tau_g$ and $\Gamma_e=1/\tau_e$ are adequate for the irreversible part of the equations of motion. We will take the dephasing rates fitted to the experimental data; compare Sec. II. For the thermalization rates between the occupations, we assume the same emission and absorption rates for all vibrational levels within the same oscillator potential and relate emission and absorption rates by a Boltzmann factor

$$\gamma_e^{\mathrm{abs}}=e^{-\hbar\omega_e/k_BT}\gamma_e^{\mathrm{em}},$$
$$\gamma_g^{\mathrm{abs}}=e^{-\hbar\omega_g/k_BT}\gamma_g^{\mathrm{em}}. \tag{29}$$

Charge conservation is achieved by treating the thermalization rates as source terms for the neighboring vibrational levels, e.g., for transitions between ground-state oscillator levels

$$\frac{d}{dt}[\rho_{si,si}(t)]_{\mathrm{irr}} = -(\gamma_g^{\mathrm{em}}+\gamma_g^{\mathrm{abs}})\rho_{si,si}(t) + \gamma_g^{\mathrm{em}}\rho_{s(i+1),s(i+1)}(t) + \gamma_g^{\mathrm{abs}}\rho_{s(i-1),s(i-1)}(t). \tag{30}$$

Furthermore, we generalize the relation between the dephasing rate Γ and the transition rate γ for fermions, $\Gamma=\gamma/2$,[46] to the equations

$$\Gamma_g=\frac{1}{2}(\gamma_g^{\mathrm{em}}+\gamma_g^{\mathrm{abs}}),$$
$$\Gamma_e=\frac{1}{2}(\gamma_e^{\mathrm{em}}+\gamma_e^{\mathrm{abs}}). \tag{31}$$

With this procedure, we can relate both dephasing and thermalization rates to the damped oscillations fitted to the experimental result; compare Eq. (2). The above absorption and emission rates guarantee that the final distribution will be thermal. More complicated rates, e.g., depending on the index of the vibrational level, can be found from a detailed knowledge of the neglected couplings in the model Hamiltonian or from an elimination of Langevin forces.[47] As the only rates we can extract from the experimental results are the dephasing rates, the above scheme of Eqs. (29) and (31) was found to be most convenient. A discussion of possible broadening mechanisms can be found in the work of Sparks *et al.*[23]

Numerical results based on the above dephasing and thermalization rates are presented in Figs. 5 and 6. The data are plotted as a function of time after the pump pulse maximum using the experimental pulse length and photon energy. In the calculation, we used a pulse fluence, resulting in a total change of occupation of 10%, and an *x*-polarized pump field, so that the investigation of $\rho^{(2)}_{xj,xl}(t)$ is sufficient.

The initial change of the upper vibrational level occupations in Figs. 5(a) and 5(b) shows a maximum around $|7_e\rangle$, resulting from a combination of a resonance condition with the laser and large Franck-Condon overlap with the thermally occupied lowest vibrational levels $|i_g\rangle$. After 10 ps, the distribution over different vibrational levels $|j_e\rangle$ is still far from the final thermal distribution, so that thermal equilibrium over the excited state vibrational levels is not reached within the time range investigated in the experiment. This is already evident from the average number of quanta in the initial distribution: It is about 8 higher than in the thermal distribution with $\overline{n}=1.37$. The initial loss rate of oscillator quanta is of the order of $\gamma_e^{\mathrm{em}}-\gamma_e^{\mathrm{abs}}=0.54\Gamma_e\approx 1/\mathrm{ps}$ and slows down with time when approaching a thermal distribution.

In Figs. 5(c) and 5(d), the strongest initial change of the vibrational level occupations corresponding to the electronic ground state does not occur for the thermally most occupied level $|0_g\rangle$, but because of the somewhat off-resonant photon energy of 1.75 eV, the higher levels are subject to a more resonant coupling, so that the resonance condition overcompensates the smaller thermal occupation. The largest contribution to the transient excitation turns out to be from the vibrational level $|2_g\rangle$. Finally, the thermalization between

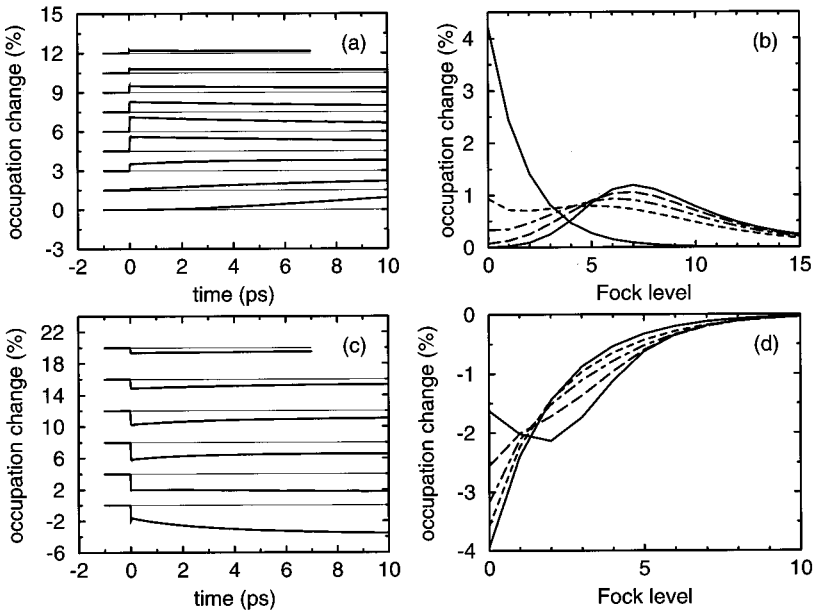

FIG. 5. Changes of vibrational level occupation for excitation with a pump pulse of 15-fs duration, photon energy of $\hbar\omega^{pu}=1.75$ eV, and maximum at zero time. The total change of occupation is 0.1. (a) $\rho^{(2)}_{xj,xj}(t)$ for different vibrational levels $|j_e\rangle$, with $j=0,2,4,6,\ldots,16$ (from bottom to top). The curves are shifted for clarity. (b) Change of occupation as a function of vibrational level index for different times after the pump pulse maximum: 50 fs (solid, peaked curve), 2 ps (long-dashed curve), 5 ps (long-dashed–short-dashed curve), 10 ps (short-dashed curve), and final thermal distribution for $\tau\rightarrow\infty$ (solid curve, exponential). (c) $\rho^{(2)}_{si,si}(t)$ for different vibrational levels $|i_g\rangle$, with $i=0-5$ (from bottom to top). (d) Same as (b), but for the ground-state vibrational levels.

different levels accumulates the largest change in the lowest level, as shown in Figs. 5(c) and 5(d). As the initial number of excess quanta compared to the thermal distribution is only about 0.9, the curves after 5 and 10 ps are already rather close to a thermal distribution. The equilibrium that will be reached eventually due to the emission and absorption of oscillator quanta is only relevant for an intermediate time scale because the total ground-state occupation remains unchanged. The final equilibrium will be obtained through recombination processes from the electronic excited state to the ground state on a much slower time scale. The average energy of absorbed photons is 1.80 eV, which is larger than the pulse energy of 1.75 eV because the pulse is off resonant compared to the absorption peak in Fig. 4(b), so that its most energetic part is absorbed with higher probability.

For the correlations $\rho_{xj,x(j+1)}(t)$ shown in Fig. 6(a) as a function of time, the initial amplitudes are close to the occupations $\rho_{xj,xj}(t)$ and $\rho_{x(j+1),x(j+1)}(t)$ because the Franck-Condon factors corresponding to consecutive levels are close to each other $|F_{ij}|\approx|F_{i,(j+1)}|$. The correlations $\rho_{xj,x(j+1)}(t)$ and $\rho_{x(j+1),xj}(t)$ are complex conjugates, except for a possible sign change due to sign conventions for the wave functions of the oscillator eigenstates. Therefore, the real parts shown apply to both. After the initial oscillation amplitude has been fixed during the excitation process, the subsequent dephasing changes all amplitudes in the same way. Therefore, only the correlations after 150 fs are shown in Fig. 6(b), a time corresponding approximately to the largest extremum of the oscillations. The correlations between vibrational levels $|i_g\rangle$ and $|(i+1)_g\rangle$ are shown in Fig. 6(c) and their values after 150 fs in Fig. 6(d). Again, the initial amplitudes are close to the initial changes of the occupations $\rho_{si,si}(t)$ and $\rho_{s(i+1),s(i+1)}(t)$ in Fig. 5(d) because of similar Franck-Condon factors.

One should keep in mind that the quantities in Figs. 5 and 6 are not directly observable, but that they enter the equation of motion of the transition matrix elements needed for the calculation of the nonlinear absorption. This third and last step of the iteration in orders of the electric field of the femtosecond pulses is performed using the elements of the density matrix of second order in the pump field as saturation terms in Eq. (18) on the rhs with the electric field of the probe $E^{\rm pr}$. The resulting transition matrix elements are then of order $(E^{\rm pu})^2E^{\rm pr}$:

$$\left(\frac{\partial}{\partial t}-i(\omega_{ej}-\omega_{gi})+\Gamma\right)\rho^{(3)}_{xj,si}(t,\tau_d)$$
$$=\frac{id}{\hbar}E^{\rm pr}_x(t,\tau_d)\left(\sum_l F_{il}\rho^{(2)}_{xj,xl}(t)-\sum_k F_{kj}\rho^{(2)}_{sk,si}(t)\right)$$
$$+\frac{id}{\hbar}E^{\rm pr}_y(t,\tau_d)\sum_l F_{il}\rho^{(2)}_{xj,yl}(t)$$
$$+\frac{id}{\hbar}E^{\rm pr}_z(t,\tau_d)\sum_l F_{il}\rho^{(2)}_{xj,zl}(t). \qquad (32)$$

The second-order density-matrix elements in the last two lines on the rhs vanish for x-polarized pump field, so that the only second-order correlation in the upper oscillator potential contributing to the source terms is $\rho_{xj,xl}$. The corresponding equation of motion for $\rho_{yj,si}$ reads

$$\left(\frac{\partial}{\partial t}-i(\omega_{ej}-\omega_{gi})+\Gamma\right)\rho^{(3)}_{yj,si}(t,\tau_d)$$
$$=\frac{id}{\hbar}E^{\rm pr}_y(t,\tau_d)\left(\sum_l F_{il}\rho^{(2)}_{yj,yl}(t)-\sum_k F_{kj}\rho^{(2)}_{sk,si}(t)\right)$$
$$+\frac{id}{\hbar}E^{\rm pr}_x(t,\tau_d)\sum_l F_{il}\rho^{(2)}_{yj,xl}(t)$$
$$+\frac{id}{\hbar}E^{\rm pr}_z(t,\tau_d)\sum_l F_{il}\rho^{(2)}_{yj,zl}(t). \qquad (33)$$

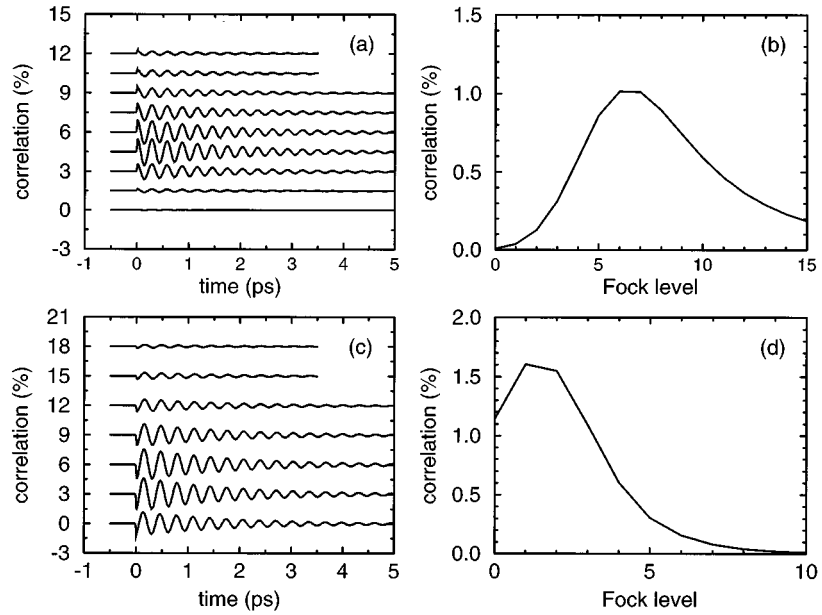

FIG. 6. Time dependence of correlations between consecutive vibrational levels, for the same pulse parameters as in Fig. 5. Only the real parts of the correlations are shown. (a) $\rho^{(2)}_{xj,x(j+1)}(t)$ for $j=0,2,\ldots,16$ (from bottom to top), with the curves shifted for clarity. (b) Amplitudes of the correlations in (a) as a function of vibrational level index j, 150 fs after the pump pulse maximum, corresponding approximately to the time of the largest extremum. (c) $\rho^{(2)}_{si,s(i+1)}(t)$ for $i=0-6$ (from bottom to top, curves shifted for clarity). (d) Amplitudes of the correlations in (c) as a function of vibrational level index i, 150 fs after the pump pulse maximum.

Because the pump was assumed to be x polarized, all second-order correlations between excited-state vibrational levels on the rhs vanish. The contribution of $\rho_{sk,si}$ to the source terms occurs in both Eqs. (32) and (33), independently of probe polarization.

The nonlinear absorption is calculated from the time-integrated power loss for delay τ_d:

$$\alpha_x^{(3)}(\tau_d)=\int_{-\infty}^{\infty} dt\; j_x^{(3)}(t,\tau_d)E_x^{\mathrm{pr}}(t,\tau_d). \tag{34}$$

$j_x^{(3)}(t,\tau_d)$ is the polarization current density calculated as the derivative of the nonlinear polarization,

$$j_x^{(3)}(t,\tau_d)=-\frac{\partial}{\partial t}P_x^{\mathrm{pr}(3)}(t,\tau_d), \tag{35}$$

which is obtained as a sum over the corresponding transition matrix elements [compare Eq. (22) for the linear polarization]

$$P_x^{\mathrm{pr}(3)}(t,\tau_d) = n_F d\sum_{i,j}\left[F_{ji}\rho^{(3)}_{xj,si}(t,\tau_d)+F_{ij}\rho^{(3)}_{si,xj}(t,\tau_d)\right]. \tag{36}$$

Because the correlations between consecutive vibrational levels in Fig. 6 are proportional to products of two different Franck-Condon factors, their sign depends on sign conventions for the wave functions. This arbitrariness has no influence on the nonlinear change of the absorption coefficient shown in Fig. 7, as products of four Franck-Condon factors occur in the calculation, eliminating the sign ambiguity of

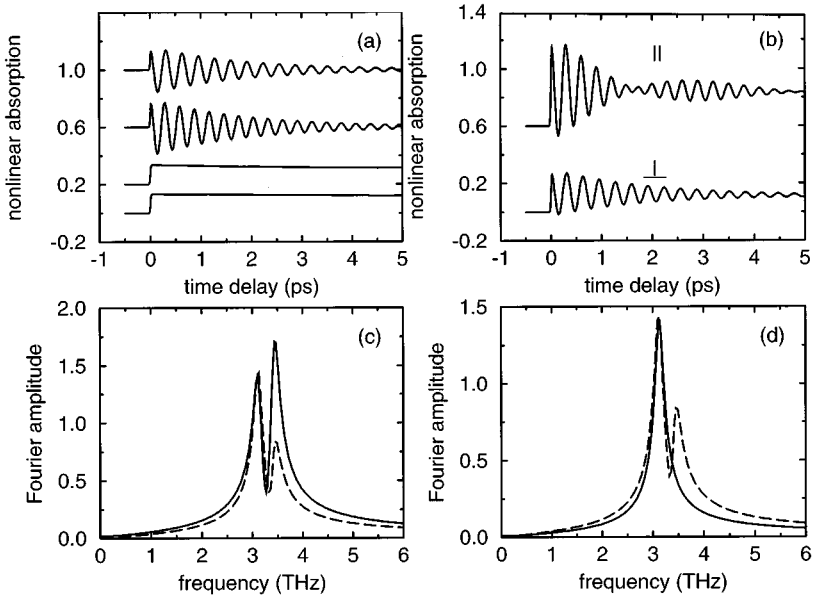

FIG. 7. Transient probe absorption as a function of time delay between pump and probe, normalized by the linear absorption. (a) Contributions to the total nonlinear absorption for $\mathbf{E}^{pr}\|\mathbf{E}^{pu}\|\mathbf{e}_x$. From bottom to top: signals due to occupation changes of vibrational levels $|j_e\rangle$, vibrational levels $|i_g\rangle$, correlations between consecutive excited-state vibrational levels $\rho_{xj,x(j+1)}$, and correlations between consecutive ground-state vibrational levels $\rho_{si,s(i+1)}$. The curves are shifted for clarity. (b) Total signal for parallel polarizations $\mathbf{E}^{pr}\|\mathbf{E}^{pu}$ ($\|$) and orthogonal polarizations $\mathbf{E}^{pr}\perp\mathbf{E}^{pu}$ ($\perp$). (c) Amplitude Fourier spectra for parallel polarizations of the two pulses calculated from the oscillating parts of the signal in (b) for delays $\tau_d>320$ fs (solid curve) and fit to measured data taken from Fig. 1(d) (dashed curve). (d) Same as (c), but orthogonal polarizations.

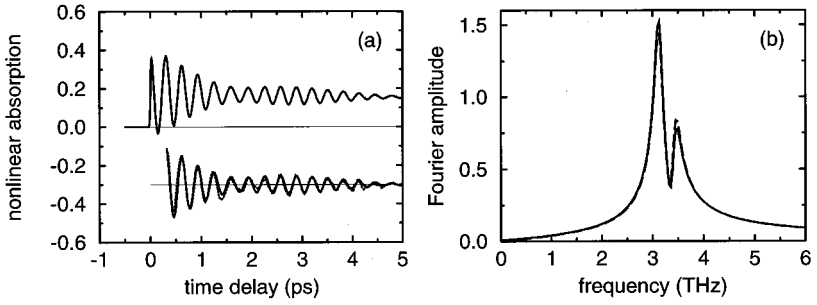

FIG. 8. (a) Absorption saturation assuming instantaneous reorientation of p states, including the 1/3 contribution of the vibrational level occupations and correlations in the excited-state oscillator potential. The lower curve is the oscillating part of this calculated signal for delays $\tau_d > 320$ fs (solid line) and superimposed the oscillating part of the measured data in Fig. 1(b), multiplied by a prefactor explained in the text (dotted line, shifted for clarity). (b) Amplitude Fourier spectrum of the oscillating part of (a) (solid line) and fit to experimental data like in Fig. 1(d) (dashed line).

the wave functions. The data in Fig. 7 are normalized to the linear absorption $\alpha^{(1)}$ of the pulse and plotted as $-\alpha^{(3)}(\tau_d)/\alpha^{(1)}$. In Fig. 7(a), we present the different contributions to the total decrease of absorption for $\mathbf{E}^{\mathrm{pr}} \| \mathbf{E}^{\mathrm{pu}} \| \mathbf{e}_x$: terms due to changes of occupations of excited- and ground-state vibrational levels and correlations between subsequent vibrational levels in the excited- and ground-state potentials, respectively. In Fig. 7(b), the total change of the absorption coefficient is shown for two different geometries: the probe field polarized parallel to the pump and the probe orthogonal to the pump polarization. In the latter case, the transient occupations and correlations in the excited-state potential do not contribute to the total signal, as mentioned after Eq. (33). Therefore, no beating pattern is observed and the decay of the oscillation is purely exponential.

The Fourier spectra in Figs. 7(c) and 7(d) are calculated only with the oscillating parts of the signal in order to eliminate the step contribution to the absorption caused by the transient diagonal occupations. As for the experimental signals in Fig. 1, the Fourier transform is calculated from the time-dependent signal for delays larger than 320 fs, eliminating the more complicated time dependence of the signal around zero delay. For parallel polarizations of the two pulses, both the correlations of consecutive vibrational levels in the ground- and excited-state oscillator potentials contribute, resulting in two peaks at the corresponding oscillator frequencies. For orthogonal pulses, only the ground-state frequency appears in the Fourier spectrum. Obviously, both curves do not correspond to the amplitude Fourier spectra of the measured signals. From the absence of signal contributions of low symmetry in the femtosecond pump-probe experiments in Figs. 1(a) and 1(b), we conclude that the orientation of the excited p states gets lost on an ultrafast time scale, so that their occupation coincides about 50 fs after the pump pulse. Here this reorientation process is included with a phenomenological reorientation rate γ_r, and the same type of reorientation is assumed for all matrix elements between vibrational levels in the excited state potential, adding on the rhs of the corresponding equation of motion, Eq. (27), the term

$$\left(\frac{d}{dt}\rho^{(2)}_{xj,xl}(t)\right)_{\mathrm{reor}} = -\gamma_r\left\{\rho^{(2)}_{xj,xl}(t) - \frac{1}{3}[\rho^{(2)}_{xj,xl}(t)+\rho^{(2)}_{yj,yl}(t)+\rho^{(2)}_{zj,zl}(t)]\right\}. \tag{37}$$

For simplicity, the corresponding rate γ_r is assumed to be infinite, i.e., the reorientation is assumed to be instantaneous, so that the matrix elements in Eq. (37) become equal and independent of pump polarization, even if only one of them, $\rho_{xj,xl}$, is coupled to a coherent source term; compare Eq. (27). This results in multiplying the contribution of the wave packet in the excited state to the nonlinear absorption by a prefactor of 1/3. This simple procedure is reasonable if the reorientation of the excited p state is much faster than 320 fs, the time delay when the part of the signal used for the calculation of the Fourier spectrum starts. From the absence of E_{1g} and T_{2g} contributions to the measured signals in Figs. 1(a) and 1(b) for delays $\tau_d > 320$ fs, it is evident that this assumption is fulfilled.

The assumed reorientation acts only on the electronic p states and has no influence on the coherence of the wave packet along the breathing mode coordinate. Therefore, it does not lead to any additional dephasing in the oscillation pattern or any change in the thermalization dynamics between consecutive breathing mode vibrational levels.

The resulting nonlinear absorption is shown in Fig. 8(a), and the corresponding Fourier spectrum in Fig. 8(b). We find excellent agreement with the measured data, which are reproduced again in Fig. 8(a). The oscillating part of the absorption saturation yields $\Delta\alpha_{\mathrm{osc}}/\alpha_0 = 0.11$ in the experiment (compare Sec. II) and $\Delta\alpha_{\mathrm{osc}}/\alpha_0 = 0.18$ in the present calculation. We conclude that the experimental excitation density is $10\%(0.11/0.18) = 6\%$, so that the present calculation up to second order in the pump field is sufficient. The calculated Fourier spectra in Fig. 8 and the spectra of the two oscillator fit taken from Fig. 1 are in excellent agreement. The differ-

ence of the calculated and measured peak ratios is below the uncertainty of the dephasing times fitted to the experimental results in Fig. 1(c).

With the simple amplitude argument derived from the ultrafast reorientation, we have a second reason to relate the higher observed oscillation frequency to the excited-state potential. The physical mechanism underlying the reorientation process is discussed in Sec. VI.

Comparing the nonlinear absorption in Fig. 8(a) calculated under the assumption of instantaneous reorientation with the experimental results in Figs. 1(a) and 1(b), we find that the relative contribution of the calculated nonoscillating part to the total signal is much too low. We suppose that the remaining part of the measured signal is due to transient phenomena related to more complicated color centers, such as F_2 and F'. A further indication that this assumption is correct comes from an aging phenomenon observed during the femtosecond experiments: The relative contribution of the oscillating part to the total transient transmission signal has decreased by a factor of 1/2 between the first experiments and the later detailed investigation of the signal contributions of different symmetry. This aging is probably due to photoinduced reactions between different types of color centers, diminishing the concentration of F centers occupied by a single electron by a factor of about 1/2. As very high intensities have to be used in femtosecond experiments, these reactions between different types of color centers are unavoidable. The photoinduced reduction of the F-center concentration by a factor of about 1/2 is in keeping with much earlier experiments.[48]

VI. TRANSIENT JAHN-TELLER EFFECT DUE TO MODES OF LOWER SYMMETRIES

As discussed in Sec. III, the Jahn-Teller modes of the lower symmetries E_{1g} and T_{2g} contribute much less than the breathing modes to the total second moment and linewidth of the absorption line; compare Table I and Fig. 3. Nevertheless, they are quite important for a complete understanding of the measured data, as they are responsible for the ultrafast reorientation introduced phenomenologically in the preceding section. If the Hamiltonian used for the breathing modes would already yield a complete description of the color center, the orientation of the p state would remain a good quantum number like in an isolated atom. This would completely change the oscillation patterns observable in a femtosecond pump-probe experiment; compare Figs. 7 and 8. Therefore, the observed ultrafast reorientation can be regarded as a manifestation of the involvement of the Jahn-Teller modes or a transient Jahn-Teller effect.

A complete investigation of the transient pump-probe experiment requires an analysis of the time evolution in a product space of the excited fermion wave functions and the oscillators that can be elongated during the optical transition, i.e., wave functions of the type

$$|p\rangle\otimes|n_1\rangle_A\otimes|n_2,n_3\rangle_E\otimes|n_4,n_5,n_6\rangle_T, \tag{38}$$

where the first part is the fermionic wave function and the other parts are products of vibrational levels of the A_{1g}, E_{1g}, and T_{2g} oscillators. Even the above wave function remains approximate because it assumes that the inclusion of a single mode of each symmetry is already sufficient. We also neglect a possible frequency shift between the electronic ground and excited states. As the dynamics of the breathing modes was already investigated in detail in Sec. V, they will be ignored in the following. This simplification is justified because the A_{1g} modes have no influence on the reorientation of the excited state. The calculation excluding the A_{1g} breathing modes requires already a five-dimensional product space of vibrational states, comprising two degenerate E_{1g} and three degenerate T_{2g} modes, multiplied by the space of excited p states. The mode energies are assumed to be $\hbar\omega_E=\hbar\omega_T=10$ meV; compare Sec. II. The Hamiltonians of E_{1g} and T_{2g} symmetries are parametrized as[49]

$$\begin{aligned}\hat{H}(E_{1g})&=\hbar\omega_E(a_2^\dagger a_2+1/2)\\&\quad+\frac{\beta}{\sqrt{3}}(2c_x^\dagger c_x-c_y^\dagger c_y-c_z^\dagger c_z)(a_2^\dagger+a_2)\\&\quad+\hbar\omega_E(a_3^\dagger a_3+1/2)+\beta(c_y^\dagger c_y-c_z^\dagger c_z)(a_3^\dagger+a_3),\end{aligned} \tag{39}$$

$$\begin{aligned}\hat{H}(T_{2g})&=\hbar\omega_T(a_4^\dagger a_4+1/2)+\zeta(c_y^\dagger c_z+c_z^\dagger c_y)(a_4^\dagger+a_4)\\&\quad+\hbar\omega_T(a_5^\dagger a_5+1/2)+\zeta(c_z^\dagger c_x+c_x^\dagger c_z)(a_5^\dagger+a_5)\\&\quad+\hbar\omega_T(a_6^\dagger a_6+1/2)+\zeta(c_x^\dagger c_y+c_y^\dagger c_x)(a_6^\dagger+a_6).\end{aligned} \tag{40}$$

The operators c and $c^\dagger$ are annihilation and creation operators for the three degenerate p states and a and $a^\dagger$ the corresponding operators for the five E_{1g} and T_{2g} oscillators. β and ζ are the elongations along the E_{1g}- and T_{2g}-oscillator coordinates when a p orbital is occupied. In the literature, several methods have been discussed to treat this problem. Minima of the potential surface for the excited p state have been investigated at several places,[50,51] and within the Franck-Condon approximation one can gain some insight into the stationary absorption line shape.[52,53] While these semiclassical calculations are only concerned with the potential surface, the full quantum-mechanical problem of finding the eigenstates is much more involved. Depending on the coupling strength of the E_{1g} and T_{2g} modes, the eigenstates can be calculated in a simpler scheme for $\beta\gg\zeta$ (Ref. 54) and for $\beta=\zeta$.[55,56] As none of these limits is fulfilled for the color center in KBr, only fully numerical methods such as the Lanczos algorithm can be used for finding the eigenstates.[56,57]

As we are mainly interested in the short-time dynamics, a direct time integration of the Schrödinger equation with the Hamiltonian $\hat{H}(E_{1g})+\hat{H}(T_{2g})$ was found to be most convenient for our purposes. We consider an eigenstate excited at time zero by a pump pulse of shape $\delta(t)$,

$$|\Psi(t=0^+)\rangle=|p\rangle\otimes|n_2,n_3\rangle_E\otimes|n_4,n_5,n_6\rangle_T, \tag{41}$$

where $|p\rangle$ is oriented according to the polarization of the pump pulse. According to the Franck-Condon principle, the vibronic part of the wave function does not have time to evolve during the excitation process, so that the only change of the total wave function at $t=0$ concerns the electronic

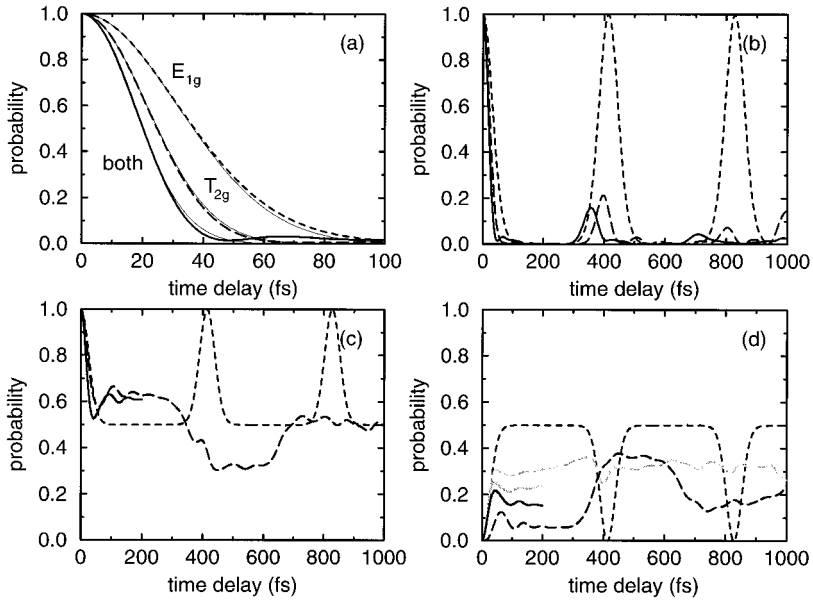

FIG. 9. Evolution of $|p\rangle|0,0\rangle_E \otimes |0,0,0\rangle_T$ in the E_{1g} subspace (short-dashed line), the T_{2g} subspace (long-dashed line), and their product space (solid lines). The pump pulse is polarized at 45° to a cubic axis. (a) Gaussian fits to the probability $|K(t)|^2$, shown as thin solid lines, with $\tau_c = 44$ fs (E_{1g}), 30 fs (T_{2g}), and 24 fs (both). (b) Same as (a), but on a longer time scale. (c) Probability to find the initial orientation $(|x\rangle + |y\rangle)/\sqrt{2}$. (d) Probabilities to find states orthogonal to the initial state. Black line, probability of $(|x\rangle - |y\rangle)/\sqrt{2}$; gray line, probability of $|z\rangle$.

part $|s\rangle \rightarrow |p\rangle$. This change switches on the symmetry-breaking Hamiltonians $\hat{H}(E_{1g})$ and $\hat{H}(T_{2g})$, and during the subsequent reversible time evolution, the factorized wave function (41) spreads over the full Hilbert space composed of the three degenerate p states and the product space of the five oscillators. As a basis, we use a sufficient number of vibrational levels for each oscillator, and it was found to be more convenient to perform the integration in the vibrational level basis corresponding to the ground state.

The broadening due to the low-symmetric modes was included phenomenologically in Eq. (24) as a frequency integral over the transition matrix elements between A_{1g} eigenstates. The Hamiltonian $\hat{H}(E_{1g}) + \hat{H}(T_{2g})$ has no influence on the A_{1g} vibrational levels $|s,i\rangle = |s\rangle \otimes |i_g\rangle$, but the states $|p,j\rangle = |p\rangle \otimes |j_e\rangle$ spread over the Hilbert space of the low-symmetric modes with time. For the time dependence of $\rho_{xj,si}(t)$ under the influence of $\hat{H}(E_{1g}) + \hat{H}(T_{2g})$, the s-symmetric part of the transition matrix element is unimportant, so that the investigation of the p-symmetric part is sufficient. It gives the additional energetic broadening related to the low-symmetric modes by the Fourier transform of

$$K(t) = \langle \Psi(0^+) | \Psi(t) \rangle, \tag{42}$$

with the wave function $|\Psi(t)\rangle$ evolving out of the initial value (41). Figure 9 shows the time evolution of the initial state $|\Psi(0^+)\rangle = [(|x\rangle + |y\rangle)/\sqrt{2}] \otimes |0,0\rangle_E \otimes |0,0,0\rangle_T$, i.e., the lowest vibrational level of the five low-symmetric oscillators after excitation with a pump pulse oriented at 45° to a cubic crystal axis. The chosen coupling constants $\beta = 13$ meV and $\zeta = 15.5$ meV correspond to the broadening parameters in Table I and Fig. 3 at zero temperature. In Fig. 9(a), Gaussian fits $|K(t)|^2 \approx \exp(-t^2/\tau_c^2)$ turn out to be a very good approximation for $|K(t)|^2 > 0.2$ and the constant τ_c in the Gaussian can be interpreted as a coherence time of the excited wave function, which corresponds to an energetic width $W = \sqrt{8 \ln 2}\hbar/\tau_c$. From the fits, we find the broadenings $W(E_{1g}) = 35.2$ meV, $W(T_{2g}) = 51.7$ meV, and $W(E_{1g}, T_{2g}) = 64.6$ meV. They are not exactly additive in the sense of Eq. (9) because the time dependences are not precisely Gaussian: The broadening due to the T_{2g} modes alone is slightly too low, while the broadening due to both E_{1g} and T_{2g} modes is slightly too high; compare Table I. We have chosen the compromise to have the correct broadening for E_{1g} modes only and all modes together within 1%, so that the broadening due to the T_{2g} modes is about 4% too low, but these deviations are well within the experimental uncertainty of 10%; compare Table I.

In Fig. 9(b), the evolution of $|K(t)|^2$ is shown on a longer time scale. The dynamics of the wave function in the two-dimensional E_{1g} subspace is periodic and behaves similarly to the evolution of a wave packet along a single oscillator coordinate. The time dependence in the three-dimensional T_{2g} subspace, on the contrary, is not periodic, so that the decay of the probability $|K(t)|^2$ looks like an irreversible phenomenon, even if it has been obtained from the reversible time evolution of the Schrödinger equation. Only partial recurrence of the initial wave function occurs, with the first maximum around 400 fs. This recurrence is further reduced when the full five-dimensional space including all the modes is considered.

In order to compare with calculations of eigenstates for a coupling to T_{2g} modes only, we have investigated $K(t)$ for several picoseconds. The structure of the absorption line calculated by Englman *et al.* for a similar coupling constant ζ is indeed reproduced by the Fourier transform of $K(t)$.[58] The initial time dependence gives the approximately Gaussian envelope of the spectrum and is a simple measure for the corresponding energetic broadening.

The corresponding time evolution of the probability to find the initial orientation $(|x\rangle + |y\rangle)/\sqrt{2}$ is shown in Fig. 9(c) and the probability to find the states orthogonal to the initial state $(|x\rangle - |y\rangle)/\sqrt{2}$ and $|z\rangle$ in Fig. 9(d). For the evolution within the E_{1g} subspace, the wave function remains in the xy plane, so that the probability to find $|z\rangle$ vanishes. Within the T_{2g} subspace and the full five-dimensional space, the time evolution of the probability to find the initial orien-

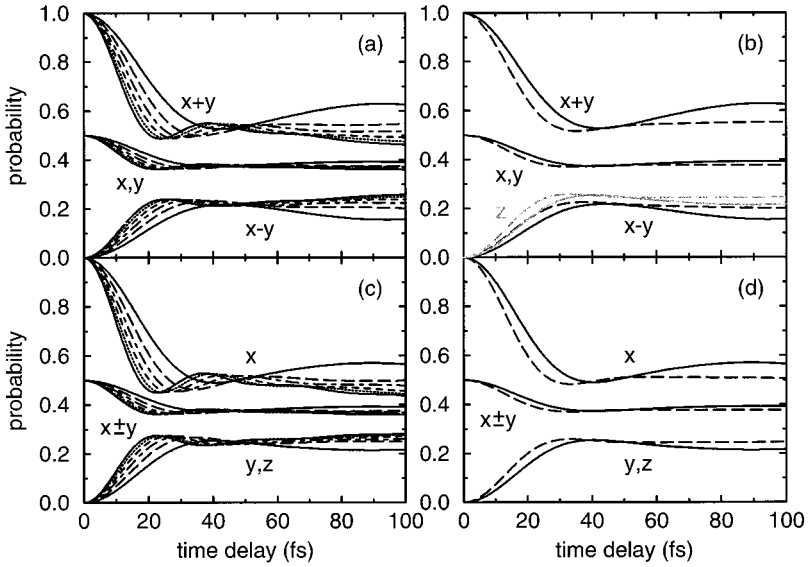

FIG. 10. Probability to find different orientations of the electronic wave function $|p\rangle$. (a) Pump field oriented at 45° to a cubic crystal axis, averages of vibrational levels for the same number of excited quanta: $n=0$ (solid line), 1 (long-dashed line), 2 (short-dashed–long-dashed line), 3 (short-dashed line), 4 (dotted line), and 5 (solid line). Probabilities of different orientations as annoted. (b) Thermal averages of the curves in (a), for $T=0$ K (solid line) and $T=77$ K (dashed line). In the latter case, 99% of the thermal probability distribution is included. (c) Same as (a), but for the pump pulse polarized along a cubic crystal axis. (d) Thermal averages of (c).

tation shows a fast initial decay within the first 50 fs, while the later dynamics are much slower. The time scale of the initial loss of orientation is about the same as for the experimentally observed vanishing of signals of T_{2g} and E_{1g} symmetries.

The essential features of the time evolution in the E_{1g} subspace in Fig. 9 can still be represented in the configuration coordinate diagram in Fig. 2. The initial state in the excited-state potential will be a coherent superposition of vibrational states having a significant overlap with the lowest vibrational level in the ground-state potential and its subsequent time evolution will be due to the oscillation in time of each vibrational level. The initial vibrational state is no longer an eigenstate in the lower potential because the Hamiltonian has changed. The wave function spreads over several vibrational levels in the lower potential with the largest extension after half a period $T_{\rm osc}/2=\pi/\omega_E$, but reaches the initial state again after a full period $T_{\rm osc}=2\pi/\omega_E$. If the number of basis vibrational levels included in the computation is too low, a significant part of the wave function reaches the highest vibrational level before half a period is over. This part is then reflected and evolves back towards the ground state, and during this time evolution, it interferes with the rest of the wave function with an erroneous phase. For the results shown in Fig. 9, vibrational levels $n_2,n_3\leqslant 16$ have been used. When the basis is reduced to nine levels, Fig. 9(b) remains nearly unchanged, but the probabilities to find different orientations in Figs. 9(c) and 9(d) develop, growing oscillatory deviations from periodicity after about 200 fs. For the T_{2g} subspace, the dynamics is not periodic, so that curves with different bases have to be compared, and a basis of $n_4,n_5,n_6\leqslant 20$ was found to be sufficient for convergence during the first picosecond. In the full five-dimensional oscillator space, the basis required for a high precision during 1 ps would in principle be the product of the bases of the subspaces, corresponding to $3\times 17^2\times 21^3=8\,029\,287$ elements. Some reduction can be achieved by eliminating vibrational levels with $n=n_2+n_3+n_4+n_5+n_6>20$, but the computational time is still prohibitive. Therefore, we restrict the investigations in the full space in Fig. 9 to a basis of 13 levels for each oscillator. This means that the full line in Fig. 9(b) is still reliable within 1% during 1 ps, but in Figs. 9(c) and 9(d) only during 200 fs.

Contrary to the pure vibrational level $|0,0\rangle_E\otimes|0,0,0\rangle_T$ investigated in Fig. 9, the experiment starts in an ensemble of thermally occupied vibrational levels. Therefore, a thermal average over initial vibrational levels has to be taken. Unfortunately, the investigation of a thermal distribution at room temperature would require a prohibitive number of initial states, so that we have to restrict the calculation to lower temperatures. At $T=77$ K, 99% of the thermal occupation probability occurs for vibrational levels up to $n\leqslant 5$, so that the total number of distinct vibrational levels (n_2,n_3,n_4,n_5,n_6) needed is 252. We restrict the following calculation to 100 fs, which turns out to be sufficient for the fastest part of the reorientation. A basis of nine vibrational levels is then sufficient for a reasonable precision.

The time evolution of different vibrational levels is shown in Fig. 10. For the assumed mode energies, $\hbar\omega_E=\hbar\omega_T=10$ meV, vibrational levels with the same number n of excited quanta are degenerate, and the curves shown in Figs. 10(a) and 10(c) are their averages. The thermal averages for $T=77$ K in Figs. 10(b) and 10(d) are calculated according to Bose-Einstein statistics and the curves for zero temperature correspond simply to the vibrational state $n=0$.

For both pump polarizations, the time evolution of the higher vibrational levels is faster. For pump field polarized at 45° to a cubic axis, the time dependences of the probabilities to find $(|x\rangle-|y\rangle)/\sqrt{2}$ and $|z\rangle$ are rather similar and only the thermal averages are shown. For pump field polarized along a cubic axis, the reorientation pattern for the states orthogonal to the pump polarization evolves on an intermediate time scale between the two cases in Fig. 10(b).

It was checked that the number of basis levels for each oscillator is of minor importance on the time scale shown: In Fig. 10(a), the probabilities for the vibrational levels with $n=5$ agreed quite well for basis length $n\leqslant 8$ and $n\leqslant 12$. The maximum deviation is below 0.08% during 50 fs and below 0.4% during 100 fs.

For $\beta=\zeta$, the relaxation behavior is isotropic, i.e., the

time dependences of orientations orthogonal to the pump polarization are equal and independent of pump polarization. This corresponds to the case investigated by O'Brien,[36,55,56] and the corresponding reorientation pattern has already been discussed elsewhere.[59]

The experimental data reveal no signals of low symmetry after about 50 fs, while the calculated probabilities in Fig. 10 do not show complete isotropy within 100 fs. This deficiency of the model calculation can be due to several reasons. The first possibility is simply related to the different temperatures. The time evolution of the higher vibrational levels occupied at room temperature could lead to a faster and more complete loss of the initial orientation.

A second possibility is that more than one mode of each symmetry occurs, involving, e.g., the shell of next-nearest neighbors of the vacancy. The coupling constant β would then be divided into several smaller coupling constants $\beta_1, \beta_2, \ldots$ for modes of E_{1g} symmetry with different frequencies, and similarly for the T_{2g} modes. An indication that this scenario could be realistic comes from the stationary Raman spectra:[16] Several structures between 6 and 20 meV are observed. One could then easily imagine that the spreading of the initial wave function over the much larger Hilbert space is more efficient for the reorientation, even if the effective coupling constant of each symmetry remains the same.

The third possibility is that the Hamiltonian $\hat{H}(E_{1g}) + \hat{H}(T_{2g})$ is oversimplified because for each symmetry only a linear coupling to the oscillator coordinate is included. More complicated terms, e.g., a bilinear coupling of oscillator coordinates to the fermion operators,[51] or cubic terms[60] are neglected. From the dephasing of the A_{1g} oscillation pattern, an estimate for typical time scales of anharmonic processes can be given: A dephasing time of 2 ps corresponds to a sum of emission and absorption rates of 1/ps; compare Eq. (31). In a five-dimensional oscillator space, the corresponding rate will be about five times faster. When a reasonable parametrization of the corresponding couplings would be known, additional parts of the Hamiltonian could easily be included in the time integration of the Schrödinger equation. An alternative would be a quantum Monte Carlo approach,[61] which has already been applied successfully to multimode vibronic problems.[62]

Even without these additional complexities, Fig. 10 demonstrates that an ultrafast reorientation does indeed occur on the time scale observed in the experiment, but because of the numerical restrictions, it remains incomplete. The fastest reorientation can be understood as the reversible evolution of the excited wave packet due to the Hamiltonian of the Jahn-Teller modes.

VII. PHASE COHERENCE AND OBSERVABILITY OF THE BREATHING MODE OSCILLATIONS

For a simple one-dimensional configuration coordinate diagram, the following condition between pulse duration τ and oscillation period $T_{\mathrm{osc}} = 2\pi/\omega$ would be sufficient for achieving a reasonable oscillatory part of the pump-probe signal:

$$\tau \lesssim \frac{T_{\mathrm{osc}}}{2}. \tag{43}$$

A similar observability condition is typically encountered for pump-probe experiments investigating bulk phonons. This simple relation is no longer valid for multidimensional oscillator spaces. Assuming one mode with a dominating contribution to the Stokes shift, the ultrafast dynamics of the other modes can destroy the initial phase of the excited wave packet, even when the coupling constants of these modes are much lower. This is precisely the situation encountered for the KBr F center.

In Sec. VI it was demonstrated that the excited-state wave function evolves out of its initial state on a very fast time scale. For the lowest vibrational level, the overlap was close to a Gaussian, with $\tau_c = 24$ fs. At higher temperatures, the corresponding thermally averaged overlap would evolve about two times faster; compare the linewidth ratios in Fig. 3. This gives a decay constant of $\tau_c = 12$ fs. When attempting the pump-probe experiment with a longer pulse, the wave function excited at the beginning of the pulse can no longer interfere constructively with the wave function excited at the end of the pulse because the initial phase gets lost due to the dynamics in the subspaces of E_{1g} and T_{2g} symmetries. This leads to a severe restriction for the observability of the oscillation pattern

$$\tau \lesssim \tau_c . \tag{44}$$

For longer pulses, the oscillation amplitude is expected to decay as a Gaussian of the pulse length.

VIII. CONCLUSION

Starting with a symmetry analysis of recent femtosecond pump-probe measurements on the KBr F center, we have developed a detailed theoretical analysis of the experimental findings. Stationary measurements of the second moment of the absorption line allowed the assignment of realistic model parameters. A density-matrix calculation for the A_{1g} breathing modes was performed and a simple amplitude argument was used for the identification of the excited- and ground-state oscillator frequencies. With the dephasing times fitted to the experimental results, quantitative agreement with the observed oscillation pattern was achieved without free parameters. The exponentially decaying part of the signal was too low in the calculation, and the remaining part of the measured signal was attributed to more complicated color centers such as F' and F_2. With a reversible calculation of the dynamics of the excited wave function in the dual space of the breathing modes, the ultrafast loss of initial orientation of the excited p state was investigated. The time scale found for this process was in agreement with the experiment, but the reorientation calculated at low temperatures remained incomplete. The loss of coherence in the dual space of the breathing modes sets a limit to the observability of the oscillation pattern: The pulse length has to be of the same order as the phase coherence time in the dual space of the mode dominating the Stokes shift.

The color center investigated here can serve as a model for the ultrafast dynamics of other defects in solids, such as the ions used for color center lasers. Furthermore, small organic molecules with a rearrangement of the atomic positions after an optical excitation will show ultrafast dynamics along only a few vibrational degrees of freedom, so that the methods used in the present calculation could possibly be applied.

ACKNOWLEDGMENTS

We would like to thank U. Grassano for the KBr samples and expert advices. Stationary measurements by V. Pellegrini and R. Fanciulli and clarifying discussions with F. Beltram are gratefully acknowledged. R.S. would like to thank Scuola Normale Superiore for hospitality during the first part of this work and the European Commission and the Deutsche Forschungsgemeinschaft for funding.

[1] M. J. Rosker, F. W. Wise, and C. L. Tang, Phys. Rev. Lett. **57**, 321 (1986).
[2] P. C. Becker *et al.*, Phys. Rev. Lett. **63**, 505 (1989).
[3] T. K. Cheng *et al.*, Appl. Phys. Lett. **57**, 1004 (1990); **59**, 1923 (1991).
[4] G. C. Cho, W. Kütt, and H. Kurz, Phys. Rev. Lett. **65**, 764 (1990).
[5] R. Scholz and A. Stahl, Phys. Status Solidi B **168**, 123 (1991).
[6] W. A. Kütt, W. Albrecht, and H. Kurz, IEEE J. Quantum Electron. **28**, 2434 (1992).
[7] T. Pfeifer *et al.*, Phys. Rev. Lett. **69**, 3248 (1992).
[8] R. Scholz, T. Pfeifer, and H. Kurz, Phys. Rev. B **47**, 16 229 (1993).
[9] A. V. Kuznetsov and C. J. Stanton, Phys. Rev. B **51**, 7555 (1995).
[10] T. Dekorsy *et al.*, Phys. Rev. B **53**, 1531 (1996).
[11] K. Leo *et al.*, Phys. Rev. Lett. **66**, 201 (1991).
[12] K. Leo *et al.*, Solid State Commun. **84**, 943 (1992).
[13] C. Waschke *et al.*, Phys. Rev. Lett. **70**, 3319 (1993).
[14] J. M. Chwalek *et al.*, Appl. Phys. Lett. **58**, 980 (1991).
[15] G. A. Russell and C. C. Klick, Phys. Rev. **101**, 1473 (1956).
[16] D. S. Pan and F. Lüty, in *Proceedings of the Third International Conference on Light Scattering in Solids*, edited by M. Balkanski, R. C. C. Leito, and S. P. S. Porto (Flammarion, Paris, 1975), p. 539.
[17] M. Leblans *et al.*, Phys. Rev. B **39**, 8657 (1989).
[18] S. E. Schnatterly, Phys. Rev. **140**, A1364 (1965).
[19] M. Nisoli *et al.*, Phys. Rev. Lett. **77**, 3463 (1996).
[20] M. Nisoli, S. De Silvestri, and O. Svelto, Appl. Phys. Lett. **68**, 2793 (1996).
[21] A. D. B. Woods *et al.*, Phys. Rev. **131**, 1025 (1963).
[22] R. A. Cowley *et al.*, Phys. Rev. **131**, 1030 (1963).
[23] M. Sparks, D. F. King, and D. L. Mills, Phys. Rev. B **26**, 6987 (1982).
[24] R. F. Wood and H. W. Joy, Phys. Rev. **136**, A451 (1964).
[25] M. Brauwers, R. Evrard, and E. Kartheuser, Phys. Rev. B **12**, 5864 (1975).
[26] M. Dominoni and N. Terzi, Europhys. Lett. **15**, 515 (1991); **23**, 39 (1993).
[27] H. A. Jahn and E. Teller, Proc. R. Soc. London, Ser. A **161**, 220 (1937).
[28] Yu. E. Perlin and B. S. Tsukerblat, in *The Dynamical Jahn-Teller Effect in Localized Systems*, edited by Yu. E. Perlin and M. Wagner (North-Holland, Amsterdam 1984), p. 251.
[29] W. B. Fowler, E. Calabrese, and D. Y. Smith, Solid State Commun. **5**, 569 (1967).
[30] R. K. Swank and F. C. Brown, Phys. Rev. **130**, 34 (1963).
[31] R. F. Wood and U. Öpik, Phys. Rev. **179**, 783 (1969).
[32] F. S. Ham, Phys. Rev. B **8**, 2926 (1973).
[33] F. S. Ham and U. Grevsmühl, Phys. Rev. B **8**, 2945 (1973).
[34] R. E. Hetrick and W. D. Compton, Phys. Rev. **155**, 649 (1967).
[35] C. H. Henry, S. E. Schnatterly, and C. P. Slichter, Phys. Rev. **137**, A583 (1965).
[36] W. Gebhardt and H. Kühnert, Phys. Status Solidi **14**, 157 (1966).
[37] I. B. Bersuker and V. Z. Polinger, in *The Dynamical Jahn-Teller Effect in Localized Systems* (Ref. 28), p. 21.
[38] R. E. Hetrick, Phys. Rev. **188**, 1392 (1969).
[39] C. Escribe and A. E. Hughes, J. Phys. C **4**, 2537 (1971).
[40] M. C. M. O'Brien, J. Phys. C **4**, 2524 (1971).
[41] S. Koide, Z. Naturforsch. **15a**, 123 (1960).
[42] D. ter Haar, *Theory and Applications of the Density Matrix*, Rep. Prog. Phys. **24**, 304 (1961).
[43] D. B. Fitchen, in *Physics of Color Centers*, edited by W. B. Fowler (Academic, New York, 1968), p. 293.
[44] W. B. Fowler, in *Physics of Color Centers* (Ref. 43), p. 53.
[45] W. T. Pollard, S.-Y. Lee, and R. A. Mathies, J. Chem. Phys. **92**, 4012 (1990).
[46] S. Mukamel, *Principles of Nonlinear Optical Spectroscopy* (Oxford University Press, Oxford, 1995).
[47] K. Lindenberg and B. J. West, *The Nonequilibrium Statistical Mechanics of Open and Closed Systems* (VCH, New York, 1990).
[48] H. Pick, Ann. Phys. (Leipzig) **37**, 421 (1940).
[49] M. Wagner, in *The Dynamical Jahn-Teller Effect in Localized Systems* (Ref. 28), p. 155.
[50] U. Öpik and M. H. L. Pryce, Proc. R. Soc. London, Ser. A **238**, 425 (1957).
[51] M. Bacci *et al.*, Phys. Rev. B **11**, 3052 (1975).
[52] Y. Toyozawa and M. Inoue, J. Phys. Soc. Jpn. **21**, 1663 (1966).
[53] K. Cho, J. Phys. Soc. Jpn. **25**, 1372 (1968).
[54] I. B. Bersuker and V. Z. Pollinger, Phys. Status Solidi B **60**, 85 (1973).
[55] M. C. M. O'Brien, J. Phys. C **9**, 2375 (1976).
[56] M. C. M. O'Brien and S. N. Evangelou, J. Phys. C **13**, 611 (1980).
[57] D. R. Pooler, in *The Dynamical Jahn-Teller Effect in Localized Systems* (Ref. 28), p. 199.
[58] R. Englman, M. Caner, and S. Toaff, J. Phys. Soc. Jpn. **29**, 306 (1970).
[59] R. Scholz, F. Bassani, and M. Schreiber, in *Excitonic Processes in Condensed Matter*, edited by M. Schreiber (Dresden University Press, Dresden, 1996), p. 211.
[60] M. Bacci *et al.*, Phys. Rev. B **12**, 5907 (1975).
[61] K. Mølmer, Y. Castin, and J. Dealibard, J. Opt. Soc. Am. B **10**, 524 (1993).
[62] B. Wolfseder and W. Domcke, Chem. Phys. Lett. **235**, 370 (1995).